Ion-beam mixing of Fe/Si bilayers

Dissertation
zur Erlangung des Doktorgrades
der Mathematisch-Naturwissenschaftlichen Fakultäten
der Georg-August-Universität zu Göttingen

vorgelegt von
Velimir Milinović
aus Belgrad, Serbia & Montenegro

Göttingen 2005

D7

1. Summary

The present study focuses on the changes in the structural and magnetic properties in Fe/Si bilayers induced by heavy-ion irradiation (^{14}N, ^{40}Ar, ^{84}Kr, ^{132}Xe, ^{197}Au). Polycrystalline Fe layers of 30-70 nm thickness were prepared by electron-gun evaporation, pulsed laser deposition or ion-beam-assisted deposition. Rutherford backscattering and Mössbauer spectroscopy, X-ray diffraction and magneto-optical Kerr effect were used as analysing techniques, as described in Chapter 3.

With respect to previous work, in which mainly noble-gas ions of low charge state and several hundred keV energy were investigated, several "non-standard" implantation conditions were considered:

(1) The use of _chemically active ions_ such as nitrogen demonstrated the competition between nitride formation and ion beam mixing at the interface (Chapter 4). During implantation only iron nitrides were formed; even at the highest nitrogen fluence no silicides were formed. After heating the irradiated samples in vacuum up to 700 ^{o}C, the iron-rich phases ε-Fe$_3$N and γ′-Fe$_4$N were formed. Starting at 600 ^{o}C β-FeSi$_2$ was identified [1-1, 2].

(2) For several noble-gas ions, the effects of _ion charge_ (e.g. 250 keV Xe$^+$ versus Xe^{17+}, 180 keV Kr$^+$ versus Kr^{11+}, 100 keV Ar$^+$ versus Ar^{8+}) and _low-energy Ar$^\pm$ pre-implantation_ into the Si wafers were studied (Chapter 5). While the interface mixing rate does not depend on the ion charge, pre-amorphization of the Si wafer enhances the mixing rate by a factor 2.

(3) Finally, experiments were conducted for _swift 350 MeV ^{197}Au^{26+}_ ions to measure the mixing rate and the magnetic anisotropy in the regime of electronic stopping (Chapter 6). A very high mixing rate of $\Delta\sigma^2/\Phi = 55$ (5) nm^4 was found and attributed to thermal spikes due to the very high energy density of about 40 keV/nm deposited in the Fe/Si couple [1-3, 4].

2. Introduction

Investigations in the field of radiation damage started sixty years ago with the advent of nuclear energy. Most of the studies in this early period were devoted to the modification of metallic compounds under neutron irradiation. Later on, the use of implantation for doping semiconductors [2-1] and producing hard coatings expanded strongly [2-2]. Finally, the formation of new phases by ion irradiation, and atomic mixing of thin films moved into focus, and it is still an active research area. Ion irradiation carried out on almost all classes of materials, from metals to living cells. As radiation induces non-equilibrium states of matter, new materials with novel properties can be created. Many applications of ion irradiation have been developed for the structuring of micro- and nano-materials of high technological interest.

2.1. Interaction of ions with solids

2.1.1.Energy loss:

When an energetic ion penetrates solid matter, it loses its kinetic energy mainly via two processes: either by elastic collision with the nuclei of the target (nuclear stopping); or inelastically by electronic excitation and ionization (electronic stopping) [2-3, 4]:

$$\frac{dE}{dx} = \left(\frac{dE}{dx}\right)_n + \left(\frac{dE}{dx}\right)_e \qquad (2.1).$$

The energy loss during interaction of the ion and the target atoms is given by:

$$(\frac{dE}{dx})_n = \sigma \cdot \frac{m+M}{4\pi e^2 Z_m Zm} \qquad (2.2),$$

where m, M, Z_m and Z are the masses and atomic numbers of the ion and target atom, respectively, and σ is the cross section for transferring the energy T from the ion to the target atom. The transferred energy T for nuclear stopping is:

$$T = \frac{4mM \sin^2\left(\frac{\phi}{2}\right)}{(m+M)^2} E_i \qquad (2.3),$$

where ϕ is the scattering angle and E_i is the initial energy of the ion.

The electronic stopping can be divided in to two regions separated by the velocity $v_o \cdot Z_i^{2/3}$, where v_o is the Bohr velocity. When the ion velocity v_i is in the range of $0.1 \cdot v_o$ to $v_o \cdot Z_i^{2/3}$, the electronic energy loss is approximately proportional to v_i (or $E_i^{1/2}$); while for $v_i > v_o \cdot Z_i^{2/3}$ the electronic energy loss is proportional to $1/v_i^2$ (or $1/E_i$). Nuclear and electronic energy losses are schematically shown in Fig 2.1.

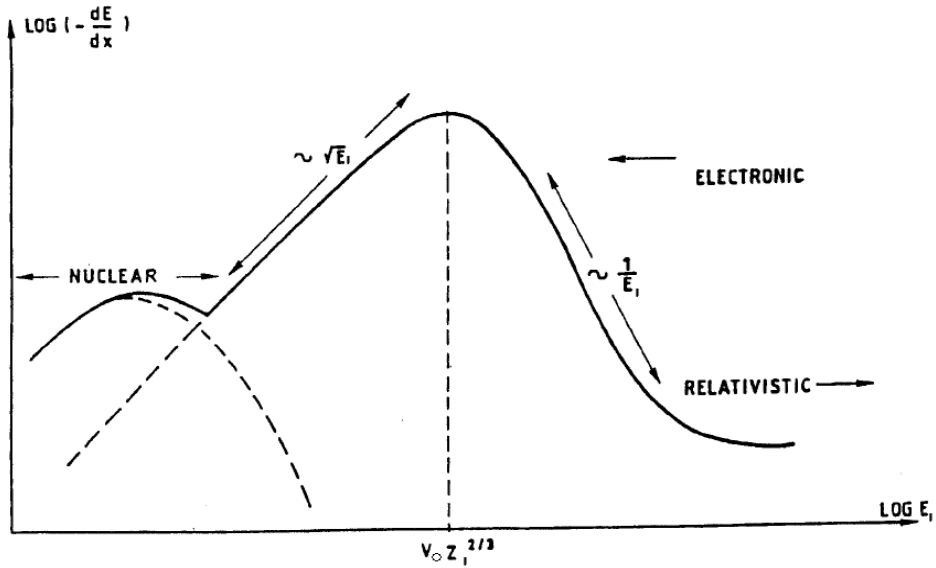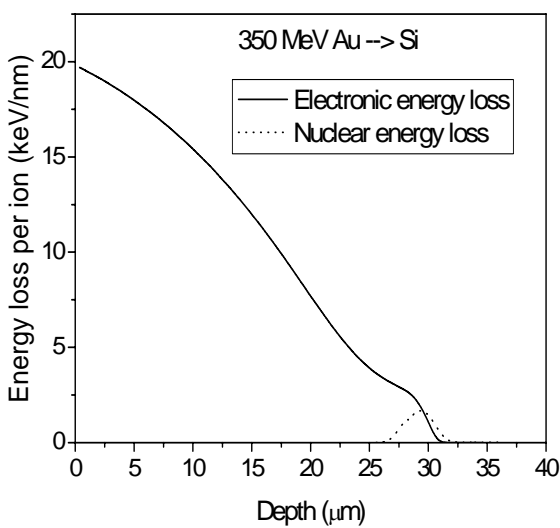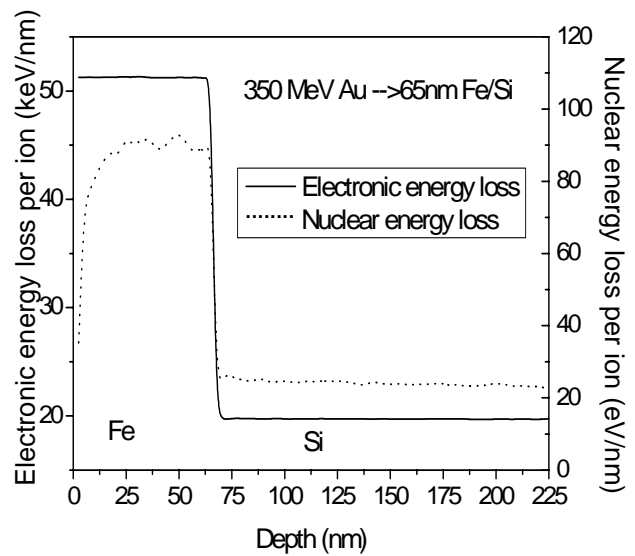Figure 2.1 Energy loss dE/dx of the ion, with energy E_i and atomic number Z_i, during penetration of a solid.

(a)   (b)

Figure 2.2 Energy loss of 350 MeV Au ion in Si (a) and 65nm Fe/Si (b).

Fig 2.2 shows the results of the Monte Carlo simulation [2-5] for nuclear and electronic losses for 350 MeV gold ions in silicon and in 65nm Fe/Si bilayer. For this ion energy in the first few micrometers electronic energy loss is dominant and about three orders of magnitude larger than for nuclear stopping.
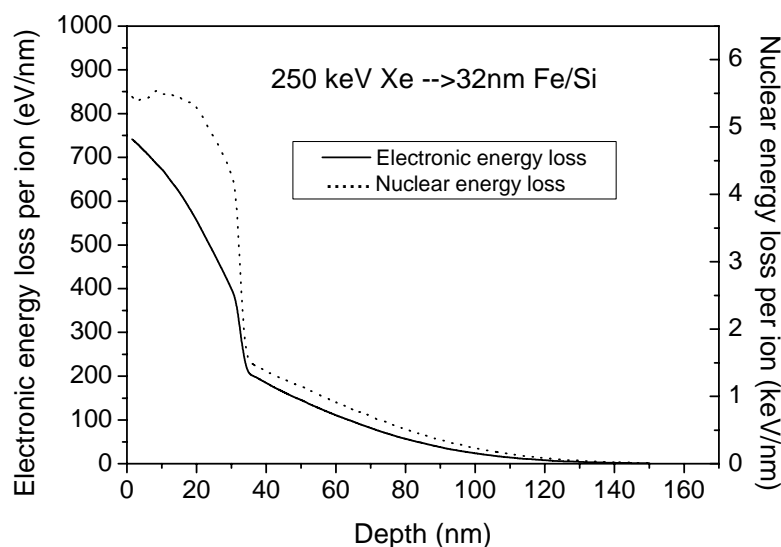
Figure 2.3 Results of the Monte Carlo simulation for nuclear and electronic loss of 250 keV Xe ions in a 32nmFe/Si bilayer.

Both energy losses remain constant over the first few hundreds of nm. At the end of the ion path, some 30 μm from the surface of the system, nuclear stopping becomes dominant. Fig 2.3. shows the situation, where nuclear loss is dominant in thin film/substrate interface region. In this figure, results of the Monte Carlo simulation for nuclear and electronic loss of 250 keV Xe ions in a 32nmFe/Si bilayer are shown. In the case of ion beam mixing experiments with 350 MeV gold ion beam, the effect of the electronic energy loss is crucial, while the thickness of the thin Fe top layer is negligible; variations of few tens of nm will not cause any change in energetic losses (Fig 2.2). On the other hand, in the case of ion beam experiments with ions in the 100 - 400 keV energy range, nuclear energy loss is dominant, and a thickness variation of the thin layer should be carefully controlled.

2.1.2. Collision cascades

Molecular dynamic simulations suggest three phases during the interaction of the energetic ion and solid: collision cascade phase, "thermal spike" phase, and relaxation phase. The collision cascade phase lasts for a few tenths of a picosecond. The primary collision between the ion and a target atom induces a series of secondary, ternary, etc., recoils, as long as the energy transfer exceeds the displacement threshold E_d. This displacement threshold is defined as the minimum energy required to produce a stable interstitial-vacancy (Frenkel) pair. Typical values of E_d are 20-30 eV. The thermal spike phase presents a specific condition of the collision cascade when all atoms in the volume of the cascade are in thermal motion. This leads to local melting, and the distribution of the atoms can be described by the Maxwell-Boltzman distribution assuming that spikes can only exist in a space-filling cascade. The upper threshold energy of the target atoms can be found [2-6]:

$$E_c = 0.039 \cdot Z^{2.23} \qquad (2.4).$$

Bearing in mind that the lower threshold energy for starting a cascade is E_d, the energy range for thermal spike formation is: $E_d < E_{projectile} < E_c$. In general, for a material with an average atomic number of less than 20, no thermal spikes are expected. The duration of a thermal spike is approximately 10^{-11} s.

The "relaxation phase" is the last phase in the collision process and represents the relaxation of the non-equilibrium regions left after the thermal spike phase.

2.1.3. Ion-beam induced mixing

Ion-beam mixing (IBM) techniques use energetic ion beams for atomic mixing of the solid materials A and B, either as bilayers or multilayers. Let us consider the case of the thin film A deposited onto a substrate B and irradiated with a heavy ion beam, assuming that the ion range is close to the thickness of film A. With properly chosen irradiation parameters a broadening of the concentration profiles ($\Delta\sigma^2$) in the interface region of materials A and B may occur. The broadening of the concentration profile ($\Delta\sigma^2$) is defined as:

$$\Delta\sigma^2 = \Delta\sigma^2_{irr} - \Delta\sigma^2_{ad} \quad (2.5),$$

where $\Delta\sigma^2_{ad}$ and $\Delta\sigma^2_{irr}$ are squares of the half the distance between 16% and 84% of the maximum concentration of a certain element in the A/B interface region (see Fig

2.4) for the as-deposited and the irradiated system respectively. In most cases the broadening of the concentration profiles is linear to the applied ion fluence:

$$\Delta\sigma^2 = k\cdot\Phi \qquad (2.6),$$

where k is the mixing rate.

A similar linear relation of the concentration profiles is obtained during thermal annealing of the A/B system is shown in Eq 2.7:

$$\Delta\sigma^2 = 2\cdot D\cdot t \quad (2.7),$$

where D is diffusivity and t is the diffusion time. The diffusivity D is given by the relation:

$$D = v\cdot\lambda^2 / 6 \qquad (2.8)$$

where v is the average velocity and λ^2 is the mean square distance of the thermally activated atomic jumps. By making the correlation between Eq 2.6
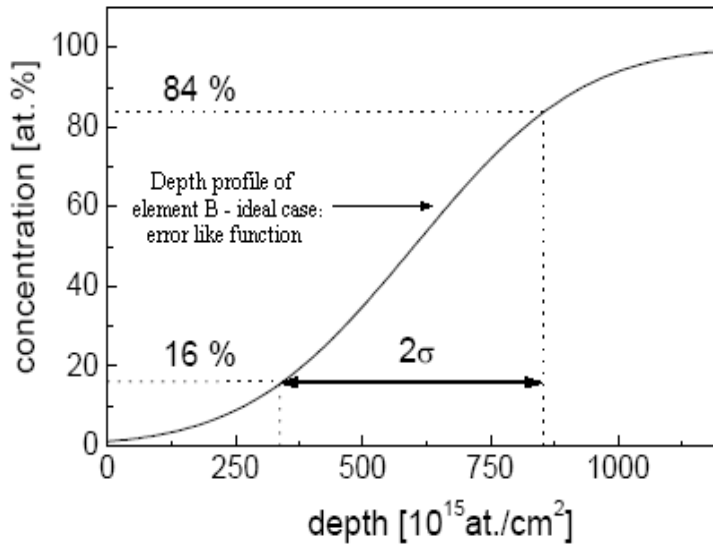
Figure 2.4 Determination of the variation of the concentration.

and Eq 2.8 and replacing v with the number of atoms replaced per fluence unit n_r/N, where n_r is the number of relocated atoms per incoming ion and path length and N is the atomic density of the target, the following relation for the mixing rate k is obtained:

$$k = \Delta\sigma^2 / \Delta\Phi = n_r / 3\cdot N\cdot\lambda_r^2 \qquad (2.9).$$

The task of all theoretical models is to find suitable expressions for the quantities n_r and λ_r which successfully describe experimental results. The basic models, dealing with the IBM process, are: the ballistic model, the global spike model and the local spike model.

a) Ballistic mixing

This model only assumes that independent binary collisions between target atoms contribute to the mixing rate k, i.e. during the ballistic cascade phase. The final relation for ballistic mixing has the following form [2-7, 8]:

$$k_{ball} = \frac{1}{3}\Gamma_0 \xi \frac{F_D R_d^2}{N E_d} \qquad (2.10),$$

where ξ is a kinematic factor, $\xi = [4mM/(mM)^2]^{1/2}$, $\Gamma_0 = 0.608$ is a dimensionless constant, N is the atomic density of the target, R_d is the minimum separation distance for the production of a stable Frenkel pair ($\approx$ 1nm). F_D is the deposited energy per ion per unit length and defined by:

$$F_D(x) = (2n_v(x)+n_r(x)) \cdot E_D \qquad (2.11),$$

where $n_v(x)$ is the number of vacancies produced per nm and $n_r(x)$ is the number of replacement collisions. The F_D values are obtained by the SRIM code.

   b) *Global spike mixing*

The model for the global spike mixing is based on the assumption of a cylindrical thermal spike around the ion path, and has the following form [2-6, 9]:

$$k_{gb} = k_1 N^{-5/3} \left(\frac{F_D}{\Delta H_{coh}}\right)^2 \left(1+\frac{k_2 \Delta H_r}{\Delta H_{coh}}\right) \quad (2.12),$$

where k_1=0.35 nm and k_2=27.4 are phenomenological constants, ΔH_r is the reaction enthalpy and ΔH_{coh} is the cohesive energy of the reaction products.

   c) *Local spike mixing*

The local spike model assumes the formation of local spherical spikes along the collision cascades [2-10]:

$$k_{ls} = k_1' \frac{Z_t^{1.5}}{N^{4/3}\Delta H_{coh}^{5/3}}(1+\frac{5}{6}k_2' \frac{\Delta H_r}{\Delta H_{coh}})F_D \quad (2.13.),$$

where the phenomenological constants k_1' and k_2' are independent of the target material.

It was found that the ballistic effects are often very small and that local or global thermal spikes dominate atomic mixing in metal/silicon bilayers irradiated with heavy ions.

2.2. The Fe-Si system

Pure iron exists in three allotropic phases: α, γ, and δ. α-Fe forms a bcc crystal structure and has an atomic weight of 55.847. The transformation point between α-Fe and γ-Fe is 911°C. γ-Fe has an fcc crystal structure and an atomic weight of 55.847. The transformation point at which bcc δ-Fe is formed is 1392 °C. The melting point of iron is at 1536 °C. At 20 °C, the density of α, γ, and δ-Fe is 7.866, 8.33,and 7.86 g/cm^3 respectively.

Silicon has a diamond crystal structure. Its melting point is at 1412 °C, its atomic weight is 28.086 and its density 2.33 g/cm^3.

The Fe-Si binary phase diagram is rather complicated, and consists of numerous compounds and solid solutions in different allotropic phases, which may coexist (see Fig. 2.5).
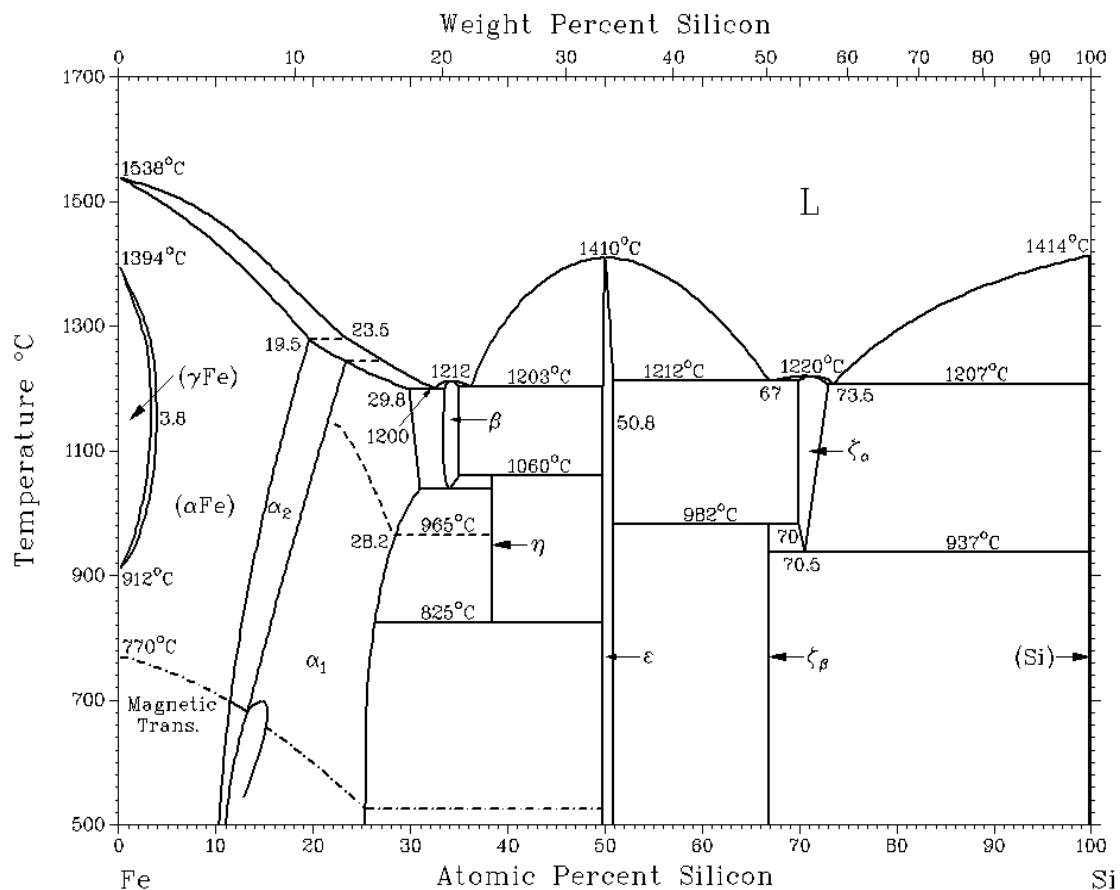
Figure 2.5 Fe-Si binary phase diagram.

Fe$_3$Si and FeSi are low-temperature phases. Iron-disilicide exists in three different phases: in a metastable cubic γ-FeSi$_2$ phase, a stable orthorhombic β-FeSi$_2$ phase, and a stable tetragonal α-FeSi$_2$ phase. FeSi (bulk unstable) and γ-FeSi$_2$ are metallic silicides. The β-FeSi$_2$ and ε-FeSi phases are semiconductors, and Fe$_3$Si and bulk unstable γ-FeSi$_2$ are magnetic compounds. The Mössbauer parameters are well documented for this system [2-11, 12, 13], which makes this spectroscopy ideal for the investigation of mixing effects.

2.3. Previous results of ion beam mixing of Fe/Si bilayers

Ion beam mixing and silicide formation in metal/silicon bilayers have been extensively studied over many years, and the Fe/Si system is no exception [2-14, 15, 16, 17, 18, 19]. All these experiments were performed with chemically non-reactive ion beams (Ar, Kr, Xe and Au), at energies ranging from 80 to 700 keV, and ion fluences between 1×10^{15} to 2×10^{16} ions/cm^2 in a wide temperature range (from liquid nitrogen temperature to 870 K). The results of the previous IBM experiments on the Fe/Si system are summarized in Table 2.1.

Table 2.1 Ion beam mixing results achieved by the previous experiments performed on the Ta/Si and Fe/Si bilayer systems.

Bilayer system	Ion	Mixing Rate $\Delta\sigma^2/\Phi$ (nm^4)				Ref
		Experimental	Ballistic	Local	Global	
42 nm Fe/Si	100 keV Ar$^+$	1.3(2)	0.16	1.3	0.4	[2-18]
31 nm Fe/Si	100 keV Ar$^+$	1.5(2)	0.18	1.4	0.5	[2-18]
33 nm Fe/Si	100 keV Ar^{8+}	2.1(2)				[2-18]
42 nm Fe/Si	250 keV Xe$^+$	4.8(5)	0.5	4	3.5	[2-17]
90 nm Fe/Si	700 keV Xe^{2+}	6.7(1.0)	0.6	4.8	4.1	[2-17]
36 nm Fe/Si	400 keV Au$^+$	8.5(1.5)	0.9	7.4	10	[2-17]

In all the cases, a linear increase in the interface variance $\Delta\sigma^2$ with the ion fluence Φ was obtained and the deduced mixing rates $k = \Delta\sigma^2 / \Phi$ were well fitted with either the local or global spike model. One of the experiments was performed on 30-40 nm thick Fe layers with Ar$^+$ and Ar^{8+} in order to check a possible influence of the ion charge state on the mixing rate, but no clear conclusion could be drawn [2-18]. Besides the Fe – Si solid solutions and the ε –FeSi phase, in some cases also the β-FeSi$_2$ phase was produced. Since this phase has interesting features (a band gap that matches the wavelength of silica optical fibers, thus making it a promising industrial material), a special effort was made to produce single-phase β-FeSi$_2$. After a fine-tuning of the experimental conditions, this aim was finally achieved [2-20].

2.4. The aim of this work

As pointed out before, most previous irradiation experiments in the Fe/Si system were performed with chemically inactive ions, and at ion energies of hundreds of keV, i.e. in the domain where nuclear stopping is dominant. In these experiments, the implanted ions served to induce or enhance atomic interdiffusion and/or phase formation via primary collisions cascades and subsequent thermal spikes. The ions were in a low charge state, and their projected range was close to the film/substrate interface.

Based on previous results, the present work aims at investigating basically novel aspects of the ion beam irradiation of Fe/Si bilayers and/or trilayers.

(a) Chapter 4 deals with the investigation on the influence of the irradiation of Fe/Si bilayers with chemically active ions, namely nitrogen, on these bilayers. We were also interested in the possibility of the formation of iron-nitride and/or silicon nitride phases during irradiation as well as during post-annealing treatments.

(b) As mentioned before, the influence of the charge state on the mixing rate of Fe/Si bilayers is not clear yet. In order to clarify this question, a careful comparison of the mixing rates obtained with highly and singly charged ions was performed for various ions (Ar, Kr, and Xe). In addition, in the same sets of experiments, the influence of the silicon surface pretreatment prior to the deposition of the iron thin film was studied (Chapter 5).

(c) The final part of this work (Chapter 6) is dedicated to studying the influence of the irradiation of the $^{nat}Fe/^{57}Fe/Si$ trilayers with swift heavy ions, namely 350 MeV Au^{17+}. In contrast to all previous experiments, here nuclear stopping is negligible, and electronic stopping plays the major role.

3. Experimental techniques

3.1. Film preparation

All the samples were made of thin solid iron films deposited on silicon wafers. The film thickness was up to 70 nm. The films were prepared by physical vapor deposition techniques: either electron gun deposition or pulsed laser deposition (PLD). Two sets of the films, with natural iron, were prepared by either electron gun deposition in Göttingen in an ultra-high-vacuum (UHV) chamber [3-1] or by Ion Beam Assisted Deposition (IBAD) chamber at the Vinča Institute , Belgrade [3-2]. Another set of samples, containing layers of ^{57}Fe, 95% isotopically enriched, were grown by pulsed laser deposition on Si (100) wafers at the Institute of Materials Physics, Göttingen University [3-3]. The last set of samples, with a 20 nm thick layer of ^{57}Fe between the top 45 nm of natural iron layer and the silicon substrate, were prepared by PLD at the Leibniz Institut für Festkörper und Werkstofffforschung (IFW), Dresden.

Before mounting the Si substrates in the deposition chambers, a standard cleaning procedure was performed: moisture was removed by ultrasonic cleaning, and after that procedure, the native oxide layers on the Si-wafer surface were removed by diluted HF and deionized water. All these precautions did not provide a contaminant-free surface of the Si wafer. At atmospheric pressure, monolayers of silicon oxide are formed almost immediately (within less than a second). Even when the wafer is mounted inside the deposition chamber, which is evacuated to the typical pressure of 10^{-8}-10^{-9} mbar, monolayers are formed within 5-30 minutes. Consequently, all samples had some degree of surface and interface contamination, mainly by H_2O vapor and/or CO_2, H_2. In order to achieve a clean surface, the Si wafers of the samples prepared in Belgrade were sputter-cleaned with a 1 keV Ar^+ ion beam prior to the deposition, but on the other hand, the pressure in the IBAD chamber was only 10^{-7} mbar, i.e. one order of magnitude lower than in the other cases.

3.2. Rutherford Backscattering Spectroscopy (RBS)

Since the first experiment with energetic alpha particles scattered from a thin gold foil was performed by Rutherford and Geiger (Nobel Prize in chemistry in 1908), the RBS technique has been under constant development and improvement and is nowadays a standard technique for analyzing depth profiles in thin films. RBS deals with the

measurement of the energies of ions backscattered from the sample. The sample is not damaged structurally during the analysis and therefore RBS is considered non-destructive. Typically, helium ions with energies of up to 2 MeV are used. From the energy of the backscattered particles the target's elemental composition can be deduced; from their intensity the target's elemental concentration can be resolved and from the energy loss of the particles in the specimen before and after the scattering, one determines the elemental depth distribution profile. The wide use of the RBS technique is due to its high sensitivity (mainly for heavy components, typically 0.1 at.% in a light matrix) and depth resolution in the nm range.

Kinematic factor

An incident beam of particles with mass m and energy E_0 is backscattered at the surface of a sample by nuclei with mass M_i. The energy of the backscattered particles only depends on M_i and three known fixed quantities: E_0, m, and the scattering angle θ, in the laboratory frame. The kinematic factor is the ratio between the energy of the backscattered and incident particles and it is given by:

$$K_i \overset{def}{=} \frac{E_i}{E_0} = \left(\frac{(M_i^2 - m^2 \cdot \sin^2 \theta)^{1/2} + m \cdot \cos\theta}{M_i + m} \right)^2 \quad (3.2.1).$$
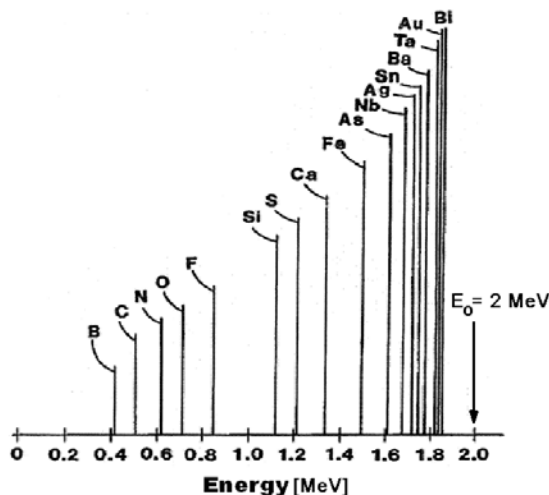

Figure 3.2.1 Mass dependence of the k factor (illustration of equation 3.2.1): m = 4, E$_o$ = 2 MeV and θ = 180°.

Hence, measuring the energy of the backscattered particle provides information on mass M_i. This equation, for the alpha particles ($m = 4$) with the incident energy $E_0 = 2$ MeV and the scattering angle $\theta = 180^o$, is illustrated in Figure 3.2.1. In this case equation 3.2.1 gets the form: $K_i = [(M_i - 4) / (M_i + 4)]^2$. When increasing the mass of the target nucleus M_i, the measured energy E_i increases, and the difference between the adjacent values of E_i decreases.

Cross-section and backscattering yield

When more than one type of nuclei is present in the sample, the relative intensity of the corresponding signals depends on their concentrations through the known differential cross-sections for Rutherford scattering into the solid angle $d\Omega$:

$$\frac{d\sigma_i}{d\Omega} = \left(\frac{Z_m \cdot Z_i \cdot e^2}{4E_0}\right)^2 \cdot \frac{4}{\sin^4\theta} \cdot \frac{\left\{\left[1-\left(m/M_i\right)^2 \cdot \sin^2\theta\right]^{1/2} + \cos\theta\right\}^2}{\left[1-\left(m/M_i\right)^2 \cdot \sin^2\theta\right]^{1/2}} \quad (3.2.2).$$

For increasing target charge Z_i, the cross section increases quadratically. Hence, for heavy masses the backscattered signal is much higher than that of lower mass nuclei. The number of detected backscattered particles N_i is given by:

$$N_i = \frac{d\sigma}{d\Omega} \cdot d\Omega \cdot Q \cdot N \cdot D_{Ef} \quad (3.2.3),$$

where Q is the total number of the incident particles, N the concentration of the target atoms and D_{Ef} the efficiency of the detector system.

Energy loss and depth scale

Light energetic incident particles, in most cases of RBS these are alpha particles, lose energy when penetrating the material, which is mainly due to electronic stopping. In backscattering spectrometry, where the elastic collision takes place at the depth d, one considers the energy loss along the inward and on the outward path (see Fig. 3.2.2). So, when a particle is scattered by a nucleus located at a certain depth d, its energy will already be reduced before the collision. Thus, the energy of the backscattered particles can be written as:

$$E_i = K_i \cdot (E_o - \Delta E(d)) - \Delta E(d / \cos\theta) \quad (3.2.3),$$

where $\Delta E(d)$ and $\Delta E(d / \cos\theta)$ are the energy loss. The depth scales are determined from energy loss values, which are given in following ref [3-4, 5]. Here, we neglected the energy dependence of $\Delta E(d)$ and $\Delta E(d / \cos\theta)$ during both paths in and out.

Kinematic Factor

$$K = \frac{E_{\text{after scattering}}}{E_{\text{before scattering}}}$$

● Incident particles m

○ Atoms in target M_i

⟨⟨⟨⟨⟨ Energy loss

Monoenergetic Incident Particles

$E = E_0$

$E = KE_0$

Detector

Backscattered Particles

Depth d

$E_{\text{loss}}^{\text{in}}$

$E_{\text{loss}}^{\text{out}}$

θ

Surface

$$E = K\left(E_0 - E_{\text{loss}}^{\text{in}}\right) - E_{\text{loss}}^{\text{out}}$$
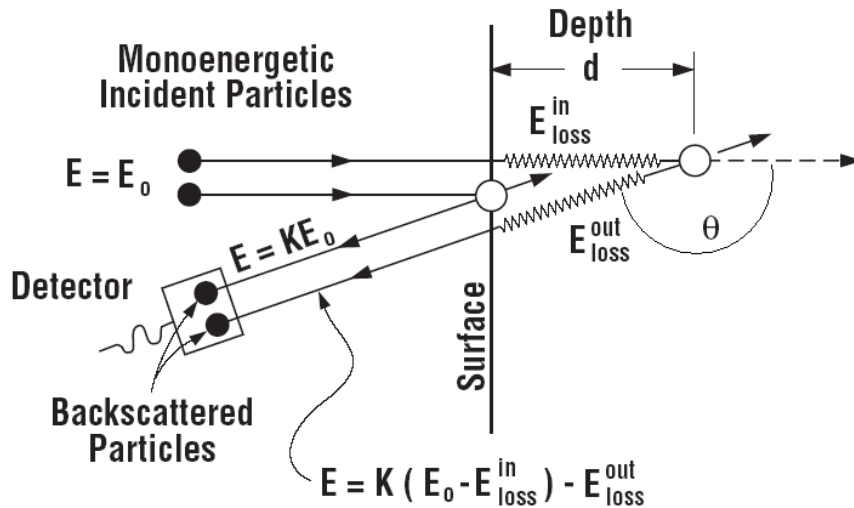
Figure 3.2.2 Schematic representation of energy loss.

All the discussed topics related to RBS can be found in the literature: [3-6, 7, 8], to name only a few of the titles.

Several RBS data analysis software packages are available, such as: RUMP [3-9], NDF [3-10] or IBA [3-11]. In this work RUMP and WiNDF (Windows version of NDF) have been used.

In the present RBS experiments, a 900 keV α - particle beam from the multipurpose IONAS accelerator [3-8, 12] was used in most cases. The scattered particles were detected at $\theta = 165^{\circ}$ to the beam. For the detection of the particles, two silicon surface detectors with a typically energy resolution of 12 - 13 keV (FWHM) and a solid angle $d\Omega$ of 3.2 msr were used. A few of the RBS experiments were performed at the University of Jena with a 1 MeV α - particle beam, with a silicon surface detector positioned at $\theta = 168^{\circ}$, and an energy resolution and solid angle of 15 keV and 3.2 msr, respectively.

As an example, a raw RBS spectrum and a fit of it, as well as the corresponding deduced depth profiles are shown in Figure 3.2.3. This thin film consists of two layers: a 20 nm thick layer of ^{57}Fe deposited on a (111) Si wafer, and a 45 nm thick layer of natural iron deposited on top of the ^{57}Fe layer. The fitting procedure was performed with the WiNDF code. In order to carry out a fit of the raw spectra, five sublayers were introduced. Each of them has a different thickness and composition, as can be seen in Table 3.2.1. For converting the at/cm^2 to the depth unit – nm, an average density of the two components was assumed.
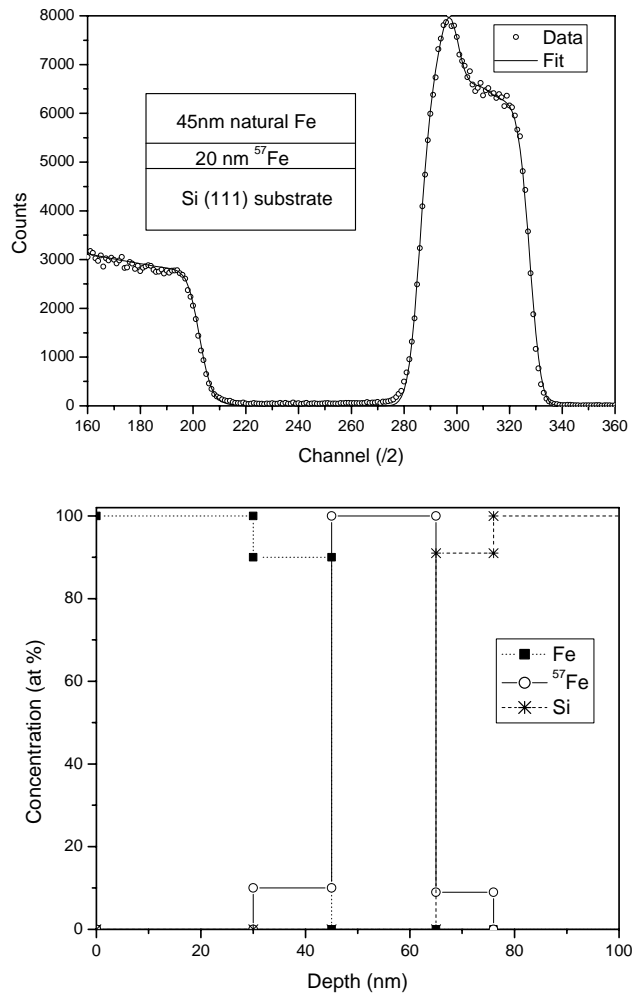

Figure 3.2.3 Example of the RBS spectra:
45 nm natural Fe/20 nm ^{57}Fe/Si (111).

Table 3.2.1 Thickness and composition of the sublayers used for the fitting procedure of the raw spectra shown in Fig. 3.2.3.

Layer	Thickness (nm)	Atomic % of $^{nat.}$Fe	Atomic % of ^{57}Fe	Atomic % of Si
1	30	100	0	0
2	17	90	10	0
3	18	0	100	0
4	11	0	9	91
5	bulk	0	0	100

17

Some of the advantages of RBS have already been mentioned, but there are also a few disadvantages. Here, two of them will be discussed briefly:

Fundamental unit of concentration obtained by RBS is in atoms/cm^2 and the concentration of the various atoms in the sample versus the backscattering energy loss. In order to convert a backscattering spectrum into a depth profile (nm unit) it is necessary to assume a density for the sample. In the case of single-element and compound films, the bulk density can be assumed for the film, and the thickness is obtained with nm accuracy. In the case of multielemental ("mixed") films with an unknown density, one may calculate the depth-dependent density of each element normalized to its concentration and incorporate this result into the WiNDF analysis. Since the RBS technique only depends on Couloumb scattering from the nuclei, in first order, it does not reveal any information on the electronic structure or chemical bonding. Implications of stoichiometric compound formation deduced from the sample composition must always be verified by other techniques, such as Mössbauer spectroscopy or X-ray diffraction.

3.3. Mössbauer spectroscopy

Mössbauer spectroscopy is based on the recoilless nuclear resonance emission and absorption of gamma rays by nuclei in solids. Its energy resolution of $\sim 10^{-12}$ is sufficient to resolve the hyperfine structures of nuclear levels, thereby making it the most precise physical measurement ever achieved. In a Mössbauer experiment only one type of isotopes is affected by the gamma-ray transition between the ground state and a specific excited state, and no other elements/isotopes contribute to the Mössbauer spectra. The traditional source of gamma rays (synchrotron radiation is "not traditional") is a radioactive source that decays into the aimed Mössbauer isotope with the following properties: long radioactive β-decay half-life (allows time to prepare and use the setup), large Mössbauer recoilless fraction for emission (Debye-Waller factor; most of the emitted gamma rays are not recoil-broadened), single-lined (without hyperfine splittings), small (intrinsic) resonance width of the transition. The intrinsic linewidth (i.e. Γ, or full width at a half maximum - FWHM) is a property of the particular transition (not depending on the host material) and is given by the relation:

$$\Gamma = \hbar/\tau \qquad (3.3.1),$$

where τ is the lifetime of the excited nuclear state.

Many isotopes have these properties, such as ^{119}Sn, ^{151}Eu, ^{129}I (see Figure 3.3.1.), but still the isotope ^{57}Fe, with its 2.2% of abundance in natural iron, is the most common Mössbauer isotope. More than 95% of all Mössbauer measurements are performed on this isotope.

1	2	3	4	5	6	7	8	9	10	11	12	13	14	15	16	17	18
H		Fe 57 14,4 2,17	Molar mass of the Mössbauer isotope, M/g mol^{-1} Mössbauer transition energy, E_γ/keV Natural abundance of the Mössbauer isotope/mass%														He
Li	Be				Highest temperature (T) of experiment reported		$T \geq 295$ K 77 K $\leq T < 295$ K $4,2$ K $\leq T < 77$ K Not observed					B	C	N	O	F	Ne
Na	Mg											Al	Si	P	S	Cl	Ar
K 40 29,4 0,012	Ca	Sc	Ti	V	Cr	Mn 55 125,9 100	Fe 57 14,4 2,17	Co	Ni 61 67,4 1,13	Cu	Zn 67 93,3 4,11	Ga	Ge 73 13,3 7,8	As	Se	Br	Kr 83 9,3 11,55
Rb	Sr	Y	Zr	Nb	Mo	Tc 99 140,50	Ru 99 89,4 12,7	Rh	Pd	Ag 109 88,0 48,16	Cd	In	Sn 119 23,9 8,58	Sb 121 37,2 57,25	Te 125 35,5 7,14	I 129 27,8 0	Xe 129 39,6 26,44
Cs 133 81,0 100	Ba 133 12,3 0		Hf 178 93,2 27,30	Ta 181 6,23 99,99	W 183 46,5 14,3	Re 187 134,2 62,60	Os 189 36,3 16,1	Ir 193 73,0 62,7	Pt 195 95,8 33,8	Au 197 77,4 100	Hg 199 158,4 16,84	Tl	Pb	Bi	Po	At	Rn
Fr	Ra		Db	Jl	Rf	Bh	Hn	Mt									

The Mössbauer Periodic Table
Data from: MERDJ. Maximum temperatures. Mössbauer Effect Reference and Data Journal, 23(6):180, 2000

	La 139 166,0 99,91	Ce	Pr 141 145,2 100	Nd 145 72,5 8,30	Pm 147 91,0 0	Sm 149 22,5 13,8	Eu 151 21,6 47,8	Gd 155 86,5 14,8	Tb 159 58,0 100	Dy 161 25,6 18,88	Ho 165 94,7 100	Er 166 80,6 33,6	Tm 169 8,42 100	Yb 170 84,3 3,05	Lu 175 113,8 97,41
	Ac	Th 232 49,8 100	Pa 231 84,2 0	U 238 44,7 99,27	Np 237 59,5 0	Pu 240 42,9 0	Am 243 84,0 0	Cm	Bk	Cf	Es	Fm	Md	No	Lr

JD Fabris
Jun 2003

Figure 3.3.1 List of isotopes suitable for Mössbauer spectroscopy.

The decay of ^{57}Fe from its parent, ^{57}Co, is shown in Figure 3.3.2. The 14.4 keV γ-ray is emitted from the excited state of ^{57}Fe via magnetic dipole transition from the I=3/2 metastable state to the I=1/2 ground state. The linewidth of the emitted gamma ray is only 4.7×10^{-9} eV.
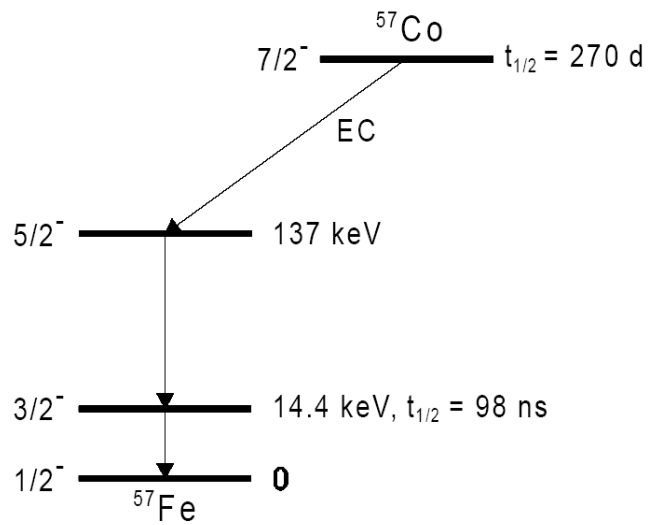

Figure 3.3.2 The decay scheme of ^{57}Co.

Apparatus

The ^{57}Fe nuclei are embedded in two solids; those in the source, which originate from the ^{57}Co decay, and those in the sample to be tested, which are in the ground state. In our case, ^{57}Co in an fcc-Rh matrix is used as a source, and the conversion electrons of the 14.4 keV transition are detected (Conversion Electron Mössbauer Spectroscopy - CEMS). The conversion electrons escape from the upper 150 nm of the sample, and in this way only provide information on thin film. In the present experiment, a triple Mössbauer spectrometer was used [3-13], but no data from transmission and conversion X-ray Mössbauer spectroscopy were recorded. The radioactive ^{57}Co source is mounted on an electromechanical drive that moves with a well-defined velocity v. Generally, velocities of a few mm/s are required. The energy of the emitted gamma rays is shifted, due to the Doppler effect, by an amount proportional to the velocity. The obtained spectrum is given in units of the Doppler velocity v, which is related to the energy shift ΔE via:

$$\Delta E = (v/c) \cdot E_\gamma \qquad (3.3.2),$$

where c is the speed of light and E_γ the Mössbauer transition energy (14.4 keV for ^{57}Fe). The conversion (and Auger) electrons were detected in a flat 2π He/CH$_4$ gas-flow proportional counter. In order to reduce the background, the amplified signals

from the detector were separated by an energy discriminator and then stored in a multichannel analyzer with 1024 channels.

<u>Hyperfine interactions</u>

There are three important hyperfine interactions detected by means of Mössbauer spectroscopy: the isomer shift, which differentiates between the ionic valence such as Fe^{2+} or Fe^{3+} and the electron density at the site of the nucleus; electric quadrupole splitting, which reflects the lattice asymmetry; and nuclear Zeeman splitting, which measures the ferromagnetic hyperfine field.

a) The simplest hyperfine interaction is the electric monopole interaction. This is due to the shielding of electrons that find themselves inside the nuclear volume. Since the nuclear site can be different for different nuclear states, the resulting energy shifts depend on the corresponding nuclear levels. The electric monopole interaction does not split the levels, but only affects their precise energies. The corresponding Mössbauer resonance is a single line called "singlet". Whenever the source and the sample have different electron densities at the nuclear site, the observed absorption occurs at some non-zero Doppler velocity. The isomer shift (IS) of the absorber relative to the source is given by:

$$IS = \text{const.} \cdot ((R^*)^2 - R^2) \cdot [\rho_a(0) - \rho_s(0)] \quad (3.3.3),$$

where R^* and R are the mean nuclear radii in the excited and ground state, respectively, and $\rho_a(0)$ and $\rho_s(0)$ are the total electron densities at the nuclei in the absorber and the source. IS can also be defined relative to a chosen calibration material, in which case $\rho_s(0)$ is the electron density at the probe nuclei of the standard. In all the CEMS measurements of this work the IS are given in comparison to α-Fe. Since only s-orbitals have a finite electron density at the nucleus, only they contribute to $\rho_a(0)$ and $\rho_s(0)$. In addition, s-type conduction electrons in metals can also contribute.

b) The electric quadrupole interaction is the hyperfine interaction between the electric quadrupole moment of the nucleus, eQ, and the local electric field gradient (EFG). The EFG is caused by the non-spherical distribution of the electrons around the probe nuclei via long range Coulomb electric forces. The EFG is a tensor described by the three componenets V_{zz}, V_{xx} and V_{yy} in the principal-axes coordinate system. As $V_{xx} + V_{yy} + V_{zz} = 0$, the EFG can be expressed by two quantities: the maximum component V_{zz} and the asymmetry parameter:

$$\eta = (V_{xx} - V_{yy}) / V_{zz} \qquad (3.3.4).$$

This interaction partially removes the degeneracies of the nuclear states. As the [57]Fe ground state has no quadrupole moment ($I = 1/2$), it is not affected by the EFG interaction. But the first excited state ($I = 3/2$) has a quadrupole moment and the degeneracy of its magnetic substates will be partially removed in the presence of an EFG. The excited state is split into two magnetic substates with magnetic quantum numbers $m = \pm 1/2$ and $m = \pm 3/2$. The splitting is called quadrupole splitting (QS, or Δ), and is given by:

$$\Delta = (e^2 qQ/2) \cdot [1 + \eta^2/3]^{1/2} \quad (3.3.5).$$

Whenever $V_{zz} \neq 0$, the Mössbauer resonance in [57]Fe consists of a doublet. The relative intensities of the two lines depend on the orientation of the EFG tensor relative to the incident gamma ray direction. For a sample in which all directions are uniformly distributed, the two lines have equal intensities (see Fig 3.3.3).

c) The magnetic dipole, or hyperfine field, interaction is the interaction between the nuclear magnetic moment and the effective magnetic field that is felt by the nucleus. This interaction completely removes all the magnetic substate degeneracy and produces a "Zeeman splitting" for the ground state (two substates with $m = \pm 1/2$) and the first excited state (four substates with $m = \pm 1/2, \pm 3/2$), and it is equal to:

$$\Delta E = g^* \mu_N B_{hf} \qquad (3.3.6),$$

where g^* is the nuclear g-factor of the considered state , μ_N is the nuclear magneton, and B_{hf} is the hyperfine field. Due to the splittings of the ground and excited state, resonance absorption can occur for six possible combinations, connected by dipole transitions. The resonance consists of six lines called "sextet".

All three hyperfine interactions are presented in Figure 3.3.3.

Literature about the Mössbauer effect can be traced since the first original work of Mössbauer [3-14], until present days [3-15, 16], which shows constant development and improvement of the Mössbauer spectroscopy.
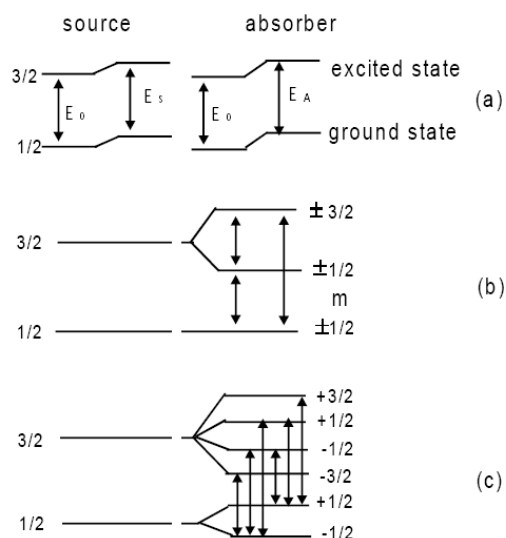
Figure 3.3.3 Schematic presentation of the energy levels and three hyperfine interactions: a) electric monopole interaction, IS b) electric quadrupole interaction, QS c)magnetic hyperfine interaction, H.

In order to fit the raw CEMS spectrum, least-square routines were used by superimposing the Lorentzian lines. The fitting procedure was performed with the Recoil program package [3-17]. The hyperfine parameters used for fitting the different phases observed in the CEMS spectrum are listed in Table 3.3.1.

Table 3.3.1 Hyperfine parameters used for fitting the CEMS spectra.
(B_{hf} = magnetic hyperfine field, IS = isomer shift, Δ = quadrupole splitting, RA = relative area of the subspectrum.)

Phase	B_{hf} (T)	IS (mm/s)	Δ (mm/s)	RA (%)	Ref.
α -Fe	33	0	0	100	
α' -Fe(N)	30.4	0.08			
ε - $Fe_{2+x}N$					
x=1.2	29.8	0.24		12	
	23.8	0.33		88	
x=1.0	28.57	0.21		11.5	
	21.83	0.33		77.0	
	7.0			11.5	[3-18, 19, 20] and references therein
x=0.67	27.4	0.26		≈3	
	20.50	0.34		61	
	9.95	0.40		36	
x=0.47	18.6	0.35		52	
	8.4	0.41		48	
γ'-Fe_4N	34.06	0.24	0.00	25	
	21.55	0.3	0.22	50	
	21.92	0.3	0.43	25	
β - $FeSi_2$	-	0.09	0.54	50	
	-	0.10	0.323	50	
amorph. Fe-Si		0.2	0.7		

23

The raw CEMS spectrum and its deconvolution are shown in Figure 3.3.4. The
hyperfine parameters used in the fitting process are listed in Table 3.3.1.
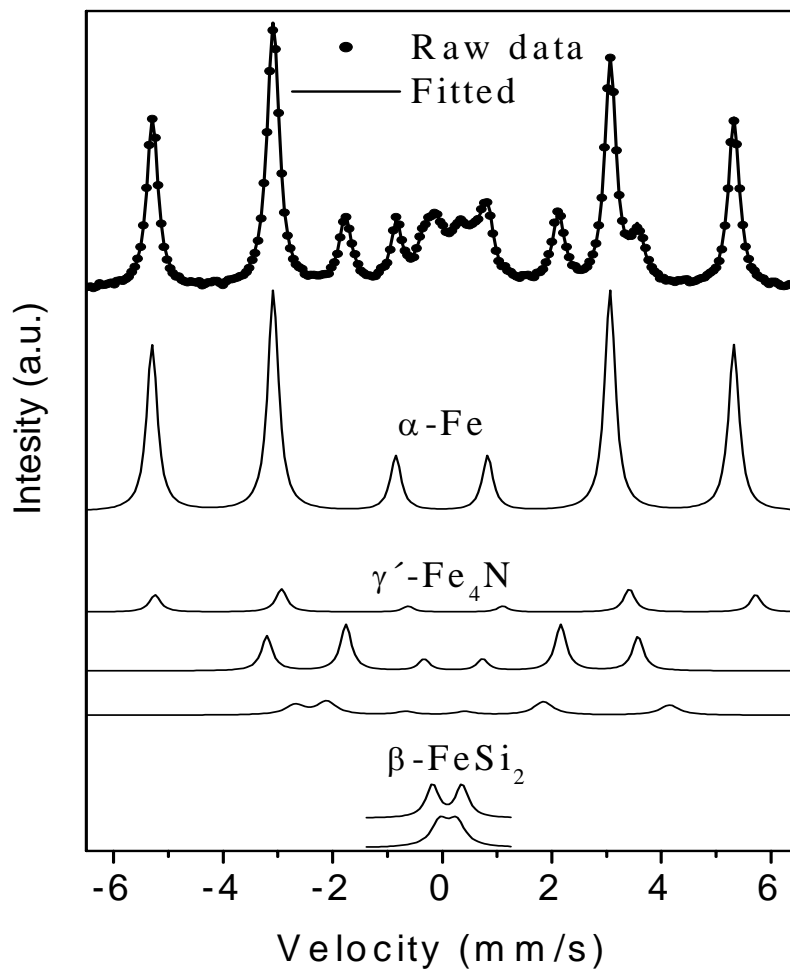
Figure 3.3.4 Deconvoluted CEM spectrum of a Fe/Si sample irradiated to the
fluence of 1×10^{17} N/cm^2 and annealed at 600°C. The subspectra corresponding to
α-Fe, γ'-Fe$_4$N and ß-FeSi$_2$ are indicated with the hyperfine parameters listed in
Table 3.3.1.

Magnetic Orientation Mössbauer Spectroscopy (MOMS)

The intensities of transitions between the magnetic substates depend on the Clebsch-Gordon coefficients of the particular transition [3-21]. Table 3.3.2 presents their values for ferromagnetic spectra in the case of ^{57}Fe:

Table 3.3.2 Intensities of the magnetic transitions in the ^{57}Fe isotope. Δm is the difference in the magnetic quantum numbers between two energy states, θ is the angle between the incident γ-ray and the principal axis of the magnetic field or the EFG tensor.

Line	Transition	Δm	Intensity
L1	$-3/2 \rightarrow -1/2$	+1	$I_1 = 3/8\ (1 + \cos^2\theta)$
L2	$-1/2 \rightarrow -1/2$	0	$I_2 = 1/2\ (1 - \cos^2\theta)$
L3	$+1/2 \rightarrow -1/2$	-1	$I_3 = 1/8\ (1 + \cos^2\theta)$
L4	$-1/2 \rightarrow +1/2$	+1	$I_4 = 1/8\ (1 + \cos^2\theta)$
L5	$+1/2 \rightarrow +1/2$	0	$I_5 = 1/2\ (1 - \cos^2\theta)$
L6	$+3/2 \rightarrow +1/2$	-1	$I_6 = 3/8\ (1 + \cos^2\theta)$

If the hyperfine field vector is in the plane of the thin film, and if the angle between the γ-ray and the sample normal is 0° ($\theta = 90^o$), the ratio of the relative intensities is:

$$I_1 : I_2 : I_3 = 3 : 4 : 1 \qquad (3.3.7).$$

If the sample is then rotated around the direction of the sample normal, the angle θ remains unchanged and the relative intensities do not change. When the geometry of the experiment is changed in such a way that the γ-ray does not enter along the surface of the sample normal, the relative intensity ratio I_1, I_2, I_3 depends on their angle, while the ratio $I_1 : I_3$ ratio remains constant. In our work we have measured the changes in the relative intensities between the sextet lines 2 and 3, which are given by the following equation [3-22, 23, 24]:

$$\frac{I_2}{I_3}(\varphi) = 4 \cdot \sum_{i=1}^{n} c_i \cdot \frac{1 - \sin^2\alpha \cdot \sin^2(\varphi - \psi_i)}{1 + \sin^2\alpha \cdot \sin^2(\varphi - \psi_i)} + 4 \cdot \left(1 - \sum_{i=1}^{n} c_i\right) \cdot \frac{1 - \cos^2\alpha}{1 + \cos^2\alpha} \quad (3.3.8),$$

where α is the angle between the γ-ray and the surface normal, φ is the rotation angle of the sample around its normal, measured from an arbitrarily chosen zero direction. The Ψ_i are the directions of the in-plane vectors of the magnetization, and c_i their relative contributions. If all hyperfine field vectors are in the film plane (i.e. $I_1 : I_2 : I_3$

$= 3 : 4 : 1$), then $\sum_{i=1}^{n} c_i = 1$, and the second term in equation 3.3.8 disappears. Finally, if the sample is tilted by $\alpha = 45^o$, equation 3.3.8 becomes:

$$\frac{I_2}{I_3}(\varphi) = 4 \cdot \sum_{i=1}^{n} c_i \cdot \frac{1 - 0.5 \cdot \sin^2(\varphi - \psi_i)}{1 + 0.5 \cdot \sin^2(\varphi - \psi_i)} \qquad (3.3.9).$$

The typical MOMS data are shown in the next few figures. These measurements were performed on the sample, which contains a 20 nm thick layer of ^{57}Fe deposited on a (111) Si wafer and covered by a 45 nm thick layer of natural iron. In order to check if all hyperfine vectors are in the film plane, first a CEMS measurement was done with the γ-rays perpendicular to the surface of the sample (Fig. 3.3.5). The spectrum was fitted with the hyperfine parameters of the α – iron, with a relative intensity ratio of: $I_1 : I_2 : I_3 = 3 : 4 : 1$.
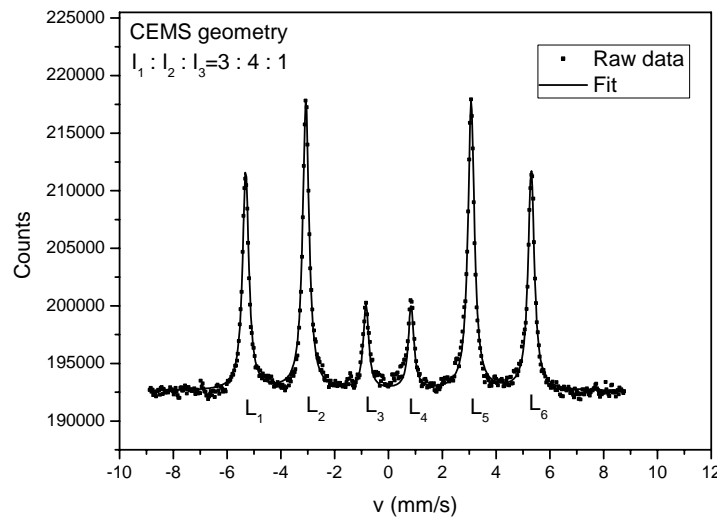
Figure 3.3.5 CEMS spectrum and coresponding fit of 45nm Fe/20nm^{57}Fe/Si.

Then, the sample was tilted by $\alpha = 45^o$ and the spectra were taken at intervals of $\Delta\varphi = 20^o$. The spectra taken at $\varphi = 120^o$ and $\varphi = 240^o$ are shown in Figure 3.3.6. Finally, a fit of the measured $I_2/I_3(\varphi)$ ratios is shown in Figure 3.3.7. Three terms of equation 3.3.9 were necessary in order to get a proper fit of the data: $c_1 = 0.35(4)$, $c_2 = 0.26(3)$ and $c_3 = 0.40(4)$ with corresponding angles of $\Psi_1 = 81(12)^o$, $\Psi_2 = 204(13)^o$ and $\Psi_3 = 310(11)^o$. Almost equal contribution of each vector, which are approximately

26

separated by 120°, indicate that the hyperfine field is almost randomly distributed in-plane.

(a)

(b)
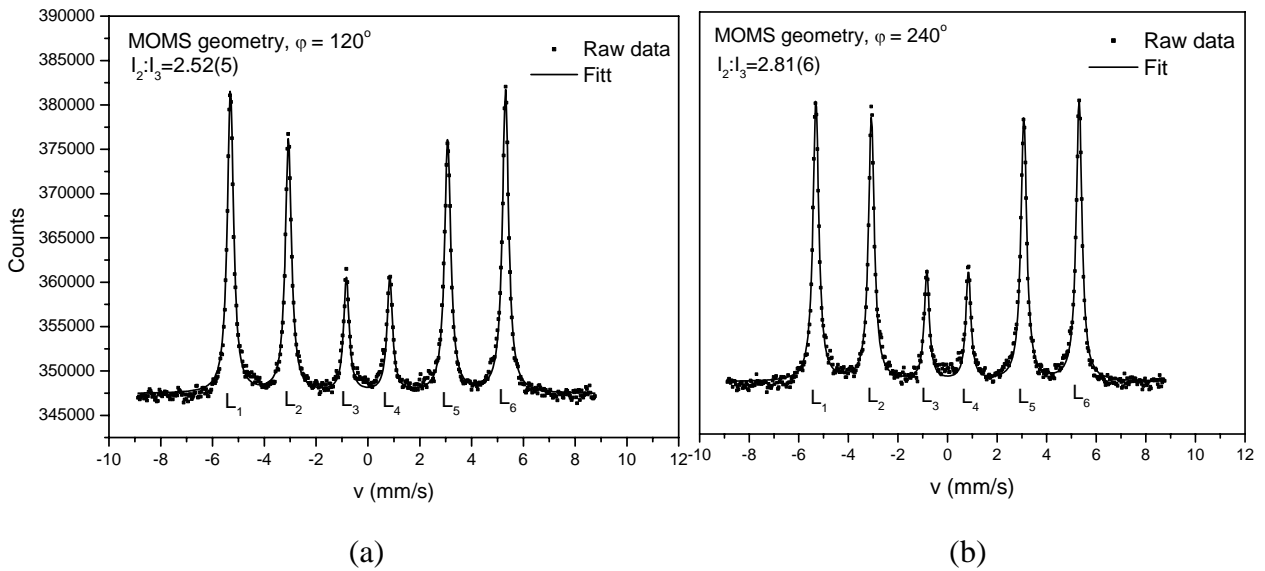
Figure 3.3.6 MOMS spectra ($\alpha = 45^\circ$) and corresponding fits for a 45nm Fe/20nm^{57}Fe/Si sample taken at $\varphi = 120^\circ$ (a) and 240° (b). The corresponding I_2/I_3 ratios are 2.52(5) and 2.81(6), respectively.
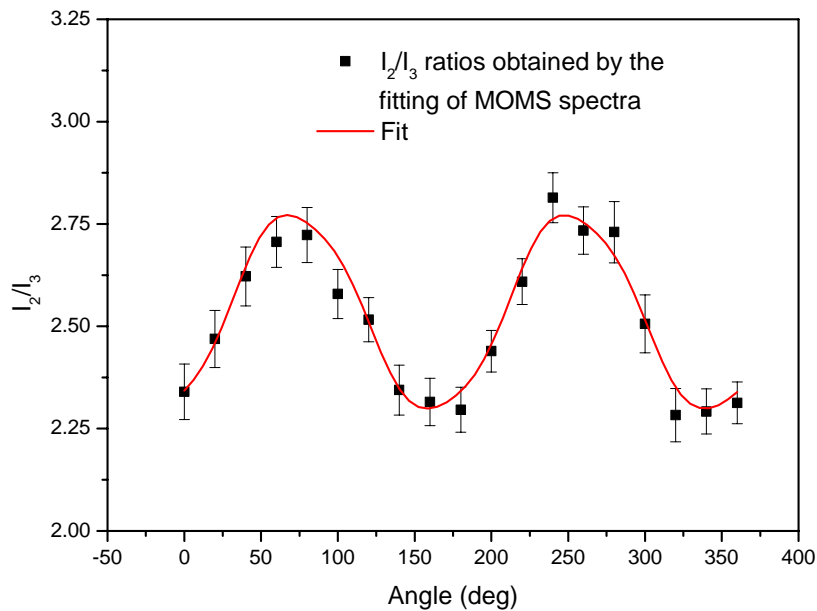
Figure 3.3.7 Relative ratios of I_2/I_3 (φ), and corresponding fit. The components of the fit are: $c_1 = 0.35(4)$, $c_2 = 0.26(3)$ and $c_3 = 0.40(4)$, with corresponding angles of $\Psi_1 = 81(12)$, $\Psi_2 = 204(13)$ and $\Psi_3 = 310(11)$.

3.4. The Magneto-Optical Kerr Effect (MOKE)

Magneto optics describes the interaction of electromagnetic radiation with magnetized matter. Magneto-optical effects are observed in a wide energy range, from microwaves through X-rays. The Faraday effect and the magneto-optical Kerr effect (MOKE) are induced by visible light, and they are linear functions of the magnetization **M**. The Faraday effect is the change in polarization that occurs upon transmission of linearly polarized light through a magnetized sample with the magnetization perpendicular to the surface [3-25]. MOKE can be observed as a change in the intensity and/or polarization of light reflected from a magnetized sample as a function of the applied magnetic field [3-26]. The Kerr signal is induced by a specific magnetization component, which is determined by the experimental geometry used. Three geometries of the MOKE effect can be distinguished (Fig3.4.1): polar, longitudinal and transversal.

| polar Kerr-effect | longitudinal Kerr-effect | transversal Kerr-effect |
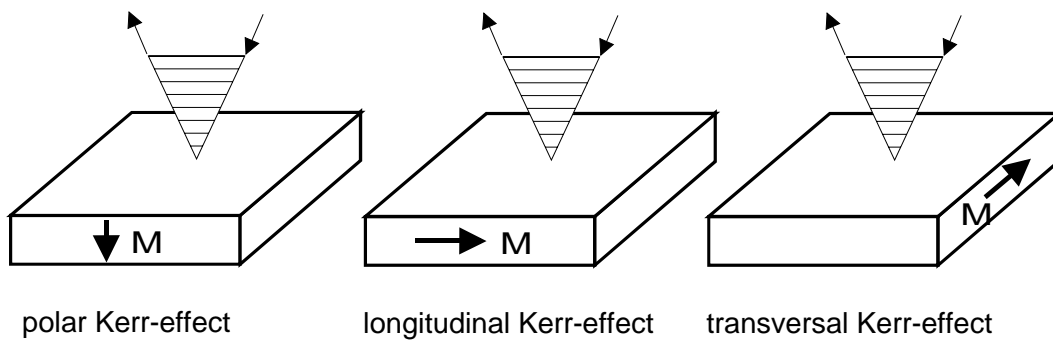
Figure 3.4.1 MOKE geometries: out-of-plane magnetization (polar); in plane magnetization with **M** parallel (longitudinal) or perpendicular (transversal) to the plane of incidence light.

For conventional MOKE measurements, the light reflected by the magnetized sample passes through an analyzing polarizer (the analyzer) and onto a photodetector, providing the signal. The nature of the Kerr effect depends on the magnetization (**M**) with respect to the scattering plane and the sample plane. When **M** is in the scattering plane and the sample plane (longitudinal orientation) or when **M** is in the scattering plane but perpendicular to the sample plane (polar orientation), the Kerr effect produces a change in the polarization state of the reflected light and the analyzer is set close to extinction in order to observe a change in the polarization state. When **M** is perpendicular to the scattering plane but in the same plane (transverse orientation), the Kerr effect is seen only as a change in the intensity of the reflected beam and the analyzer is set to transmit light of the same polarization as the incident light.

As mentioned earlier, when linearly polarized light is reflected by a magnetic film, its polarization becomes elliptic (Kerr ellipticity: $\in_{Kerr}$) and the principal axis is rotated (Kerr rotation: ϕ_{Kerr}). Both effects depend on the off-diagonal component of the conductivity tensor, polarizability tensor and frequency, and they are linear functions of **M.**

Detailed expressions for these two effects, obtained by the quantum-mechanical approach, can be found in the following references: [3-27, 28, 29]

In the present work, the longitudinal Kerr effect was used. Fig. 3.4.2 shows the MOKE set-up used in all our measurements [3-24].
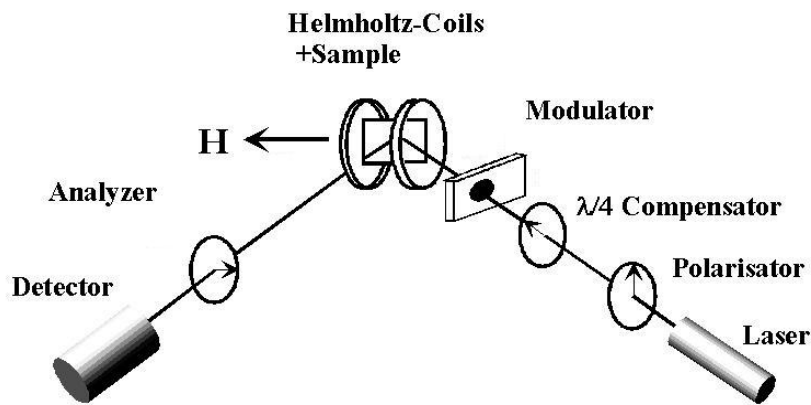
Figure 3.4.2 Schematic drawing of the MOKE set-up.

As a light source, a He-Ne laser with a power of 2 mW and a wavelength of $\lambda = 632.8$ nm was used. To adjust the polarity of the laser light, a polarisator was placed directly in the front of a laser. The polarization axis was set at 90° relative to the incidence plane of the light on the sample. Behind the polarisator, the light beam passed through a $\lambda/4$ compensator which delayed the component parallel to the slow axis of light by $\pi/2$. Before hitting the sample, the beam passed through a modulator, which changed the phase of the horizontal component of the light with a modulation frequency of 50 kHz, and the previously circular polarized light then showed a modulated linear and circular polarization. The linear polarization was oriented at $\pi/4$ after T/4 or at $3\pi/4$ after 3T/4. And the light hit the sample, which was placed in a goniometer, inside water-cooled Helmholtz coils, which provided a field strength of up to 1500 Oe. After being reflected from the magnetized sample, the light had changed its linear polarization state for $\pi/4 + \phi_{Kerr}$ (at t = T/4), or for $3\pi/4 + \phi_{Kerr}$ (at t = 3T/4). In order

to measure the Kerr effect, the reflected light was directed through an analyzer before detection. By changing the orientation of the sample via the goniometer, the intensities of the **M** vector were measured in the different direction (ϕ_{Kerr} has a linear dependence of the M!!).

As an example two hysteresis loops measured at $\varphi = 30^o$ and 90° of a 70 nm thick iron film deposited on Si wafer and irradiated with 350 Mev Au ions to a fluence of 12.5×10^{14} cm^{-2} are shown in Fig 3.4.3. The important parameters, i.e. the coercive field H_c, residual magnetization M_r and saturation magnetization M_s are also shown in this figure.
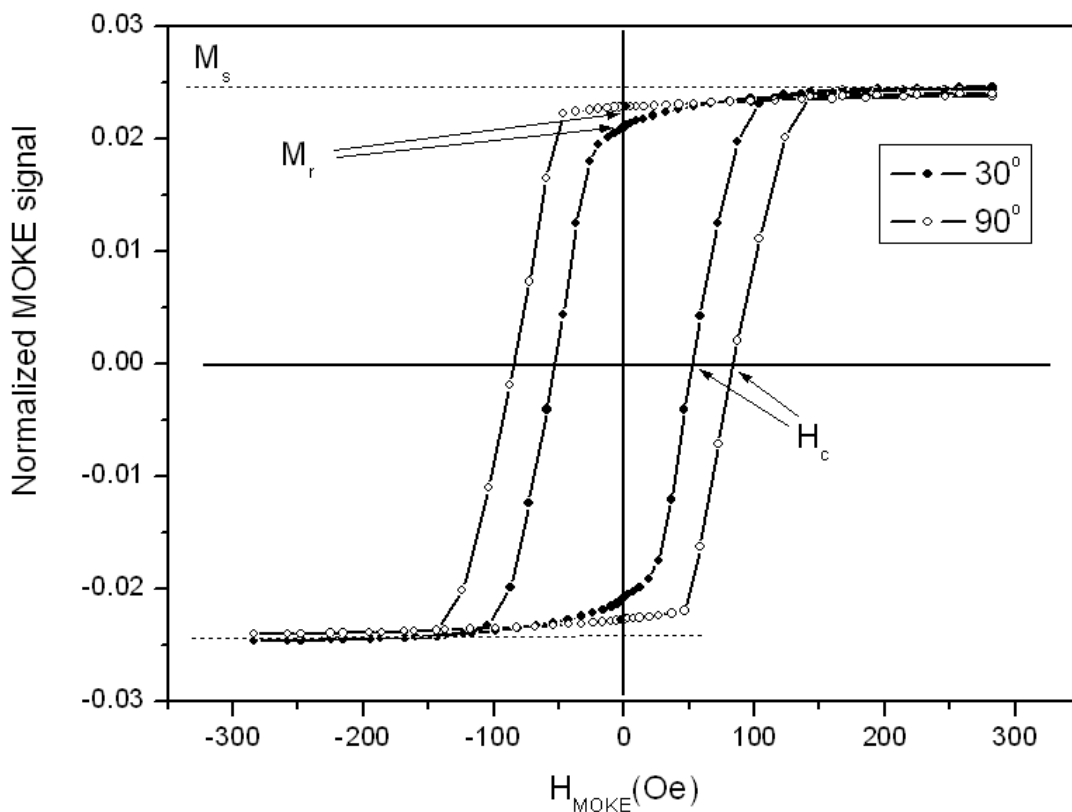
Figure 3.4.3 Hysteresis curves of the 70 nm Fe/Si sample irradiated with 350 Mev gold ions at a fluence of 12.5×10^{14} cm^{-2}. The coercive field H_c, residual magnetization M_r, and saturation magnetization M_s are also shown.

Figure 3.4.5 shows the polar plots of the quantities H_c and M_r/M_s obtained from the MOKE measurements of the same sample.
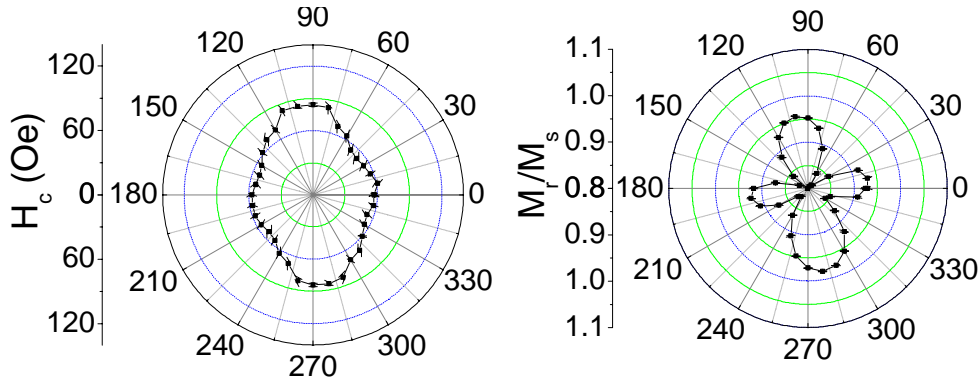
Figure 3.4.5 Polar plots of H_c and M_r/M_s obtained from the MOKE measurements of the 70nmFe/Si sample irradiated at a fluence $12.5 \cdot 10^{14}$ cm^{-2} with 350 MeV Au ions.

Visible light only penetrates some 20 nm; therefore, with MOKE only the magnetization in the surface region was probed. On the other hand, the MOMS measurements were performed on the trilayer samples, where the ^{57}Fe layer was inserted between ^{nat}Fe and the Si substrate. Hence, the biggest contribution to the MOMS spectra came from the ^{57}Fe/Si interface region, which was mixed during the ion irradiation. Therefore, a comparison of the MOKE and MOMS experiments may lead to different results.

3.5. X-Ray Diffraction (XRD)

When monochromatic X-rays hit a crystal with a wavelength comparable to the lattice constant, a constructive interference within the scattered waves may occur. The Bragg's relation gives the condition that must be fulfilled, in order to achieve constructive interference:

$$\lambda/2 = d \sin\theta \quad (3.4.1),$$

where λ is the wavelength, d is the spacing between crystallographic planes, and θ is the incidence angle of the electromagnetic waves relative to the normal of the lattice planes [3-30].

In this work, the Cu K_α line with a wavelength of 1.54 nm was used. Bragg-Brentano and grazing incidence geometries were applied. In the Bragg-Brentano geometry, the source of the X-rays and the detector are moving simultaneously, while in the grazing incidence geometry the incoming X-ray beam enters at a fixed small angle (up to 5^0) relative to the surface of the sample, and the detector is moving. In this way, the X-ray

spectra provide information on the near-surface part of the sample. The reflections were compared to the powder diffraction database [3-31], and in this way a phase analysis was done.

In Figure 3.5.1, the XRD spectrum of a trilayer sample is displayed, which consists of a 20 nm thick layer of ^{57}Fe deposited on a (111) Si wafer, and a 45 nm thick layer of natural iron deposited on top of the ^{57}Fe layer. In this case, an XRD measurement was performed in glancing incidence geometry. The incidence angle was 3°, and the scanning was done between 42° and 100.5^o, in steps of 0.05^o; the measuring time was 60 s/step. The obtained peaks were compared with the PDF JCPDS - ICDD (Powder Diffraction File Joint Committee on Powder Diffraction Standards - International Center for Diffraction Data) database [3-31]. It was found that all peaks match the reflections from the different crystallographic planes of bcc-iron, card number 06-0696. The peak around 61° degrees is an artefact.
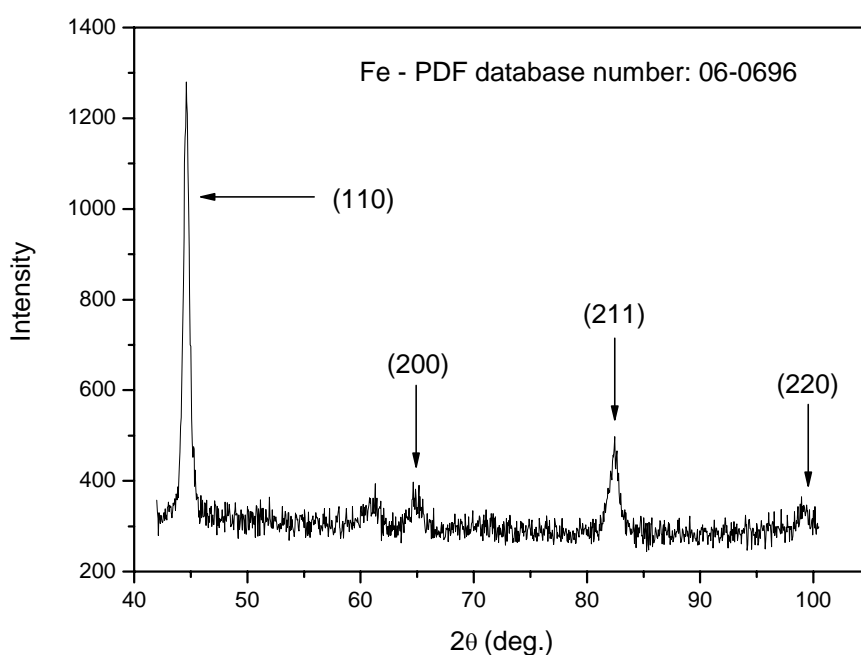
Figure 3.5.1 Glancing incidence XRD spectrum of the sample made of 40 nm natural Fe / 20 nm ^{57}Fe / Si (111).

4. Nitrogen irradiation and thermal annealing

The purpose of this part of the work is to investigate the influence of the irradiation of the chemically active nitrogen ions on the [57]Fe /Si bilayer system, as well as the influence of the post-implantation annealing treatment. Ion beam mixing of Fe/Si bilayers with noble gas ions had shown the formation of silicide phases and Fe - Si solid solutions [4-1]. In the case of high-fluence nitrogen-ion implantation across the Fe/Si interface, one may expect to see some additional iron and silicon nitride phases. Due to the important role of the Fe-N system in industry [4-2,3], its phase diagram has been under investigation for more than a century and is shown in Figure 4.1 [4-4,5].

Weight Percent Nitrogen
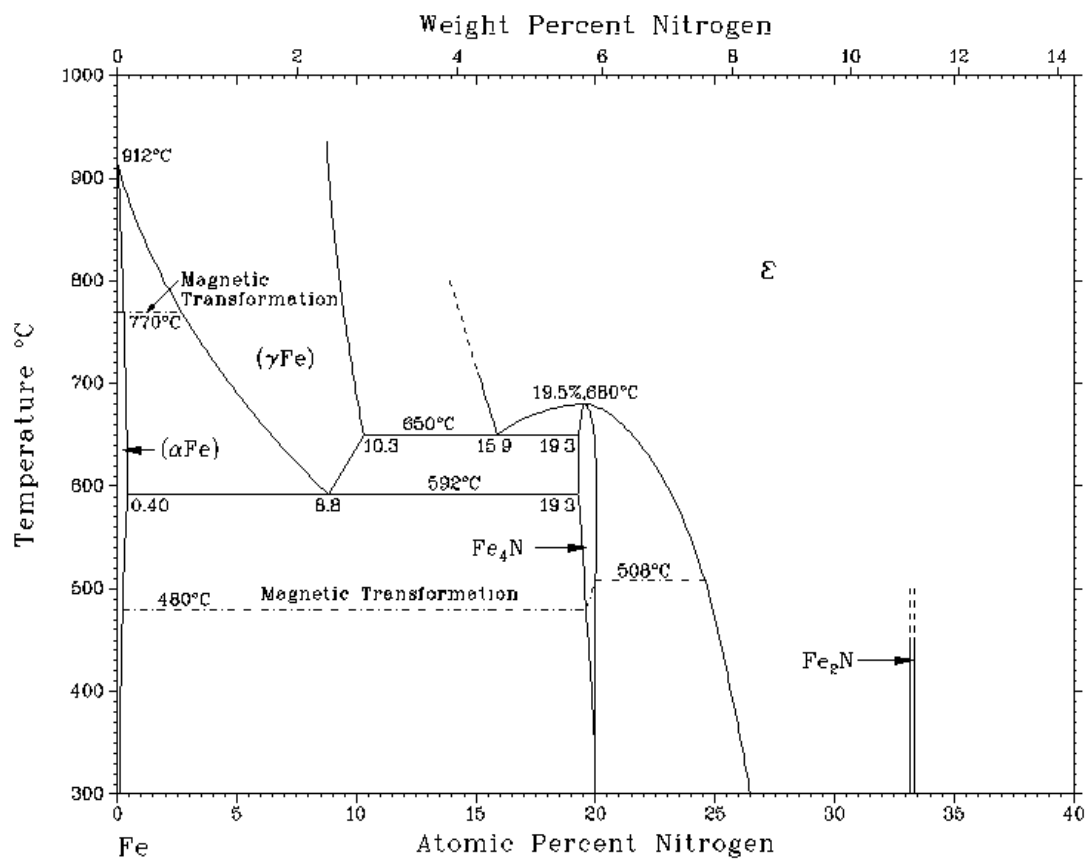
Figure 4.1 Fe – N phase diagram.

Up to about 600 ^{o}C, Fe-N system shows three solid solutions: α, γ (Fe$_4$N), ε; a chemical compound (Fe$_2$N) and two metastabile phases (α'-martensite and α''-Fe$_{16}$N). There are numerous comprehensive and well-documented Mössbauer studies about this system [4-6].

33

4.1. Sample preparation and $^{14}N^{++}$ ion irradiation

In this experiment 95% isotopically enriched ^{57}Fe - films were used. The ^{57}Fe/Si bilayers were prepared by the PLD method on Si (100) wafers. Before mounting the substrates in the deposition chamber, a standard cleaning procedure was performed, which is described in Chapter 3.1. The thin ^{57}Fe films were deposited at a rate of 0.5 nm/s at ambient temperature to a total thickness of 30 nm; the chamber pressure was below 1×10^{-9} mbar. A Kr-F excimer laser was used for the evaporation of the material [4-7].

The samples were irradiated to fluences of 0.6, 1.0 and 2.0×10^{17} ions/cm^2 with 22 keV ^{14}N^{++}-ions provided by the TESLA facility of the Vinča Institute [4-8]. The pressure in the implantation chamber and in the beam lines was better than 10^{-6} mbar. The ion current was in the range of few hundreds of nA. In order to provide a homogeneously irradiated surface, an electrostatic beam sweep-system was used.

4.2. Results and discussion

4.2.1. Phase formation

An RBS analysis was performed in order to obtain information about the film thickness, possible sputtering effects during nitrogen irradiation, and mixing at the Fe/Si interface. Figure 4.2.1 shows the RBS spectra taken from an as-deposited and irradiated ^{57}Fe/Si sample, as well as the deduced depth profiles. Comparing the integrated counts of the Fe peaks in both samples, the experimental sputtering yield was found to be less than 0.2 atoms/ion. At the highest fluence of 2×10^{17} N-ions / cm^2 only 5 nm would be sputtered off. The decrease in the height of the iron signal, with increasing nitrogen fluence, indicates significant changes in the samples. This effect is most pronounced at the highest fluence and might indicate nitride and/or silicide formation. Both the Fe and Si depth profiles show very similar results. Ion beam mixing will be discussed in Section 4.2.2.
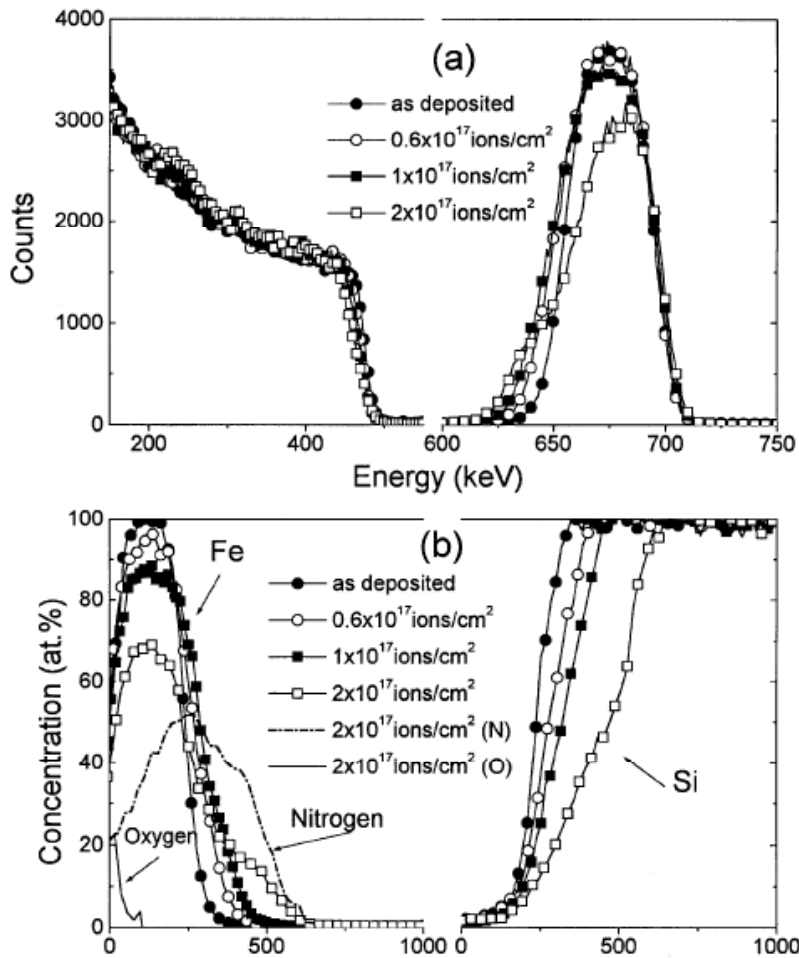
Figure 4.2.1 RBS spectra of the as-deposited and nitrogen (22 keV) irradiated samples to fluences of 0.6, 1.0 and 2.0 x10^{17} ions/cm^2 (a), as well as their corresponding calculated depth profiles (b).

As RBS was not able to provide clear information about possible nitride or silicide formation, further information about the irradiated samples was obtained by using XRD and CEM analyses.

Figure 4.2.2 shows X-ray diffraction measurements, performed at a glancing incidence angle of 5^0. As can be seen from the figure, only a few broad, peaks are recorded. A shifting and broadening of the line at an angle of 44^0 with an increasing nitrogen fluence indicates the presence of the ε-Fe$_{2+x}$N phase. This diffraction peak is broad, which suggests that the newly formed phase has small crystalline grains. At the highest fluence of 2.0×10^{17} ions/cm^2, the well defined ε-Fe$_2$N phase was achieved. In all the cases a broad peak that corresponds to the (110) Fe reflection is present. This is a clear indication that the formation of the nitride phases was not complete. No other peaks, e.g. from crystalline iron silicides, were observed.
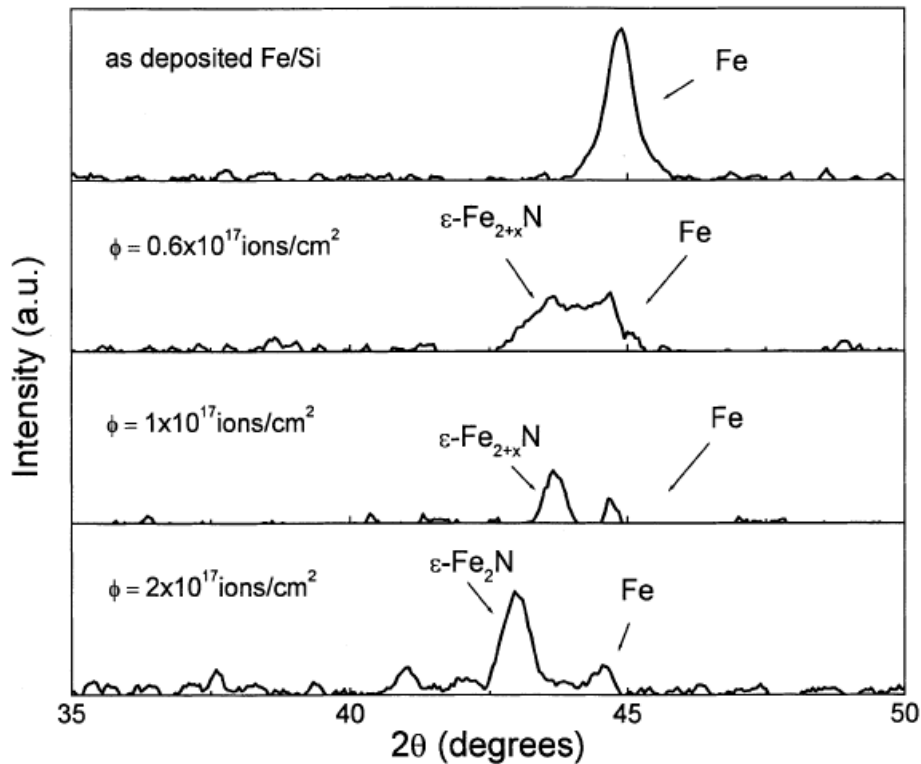
Figure 4.2.2 XRD spectra of the ^{57}Fe/Si bilayers, before and after irradiation with 22 keV nitrogen ions to various fluences.

Further information about the implanted Fe/Si bilayers was obtained by CEMS measurements. Figure 4.2.3 shows raw and fitted CEMS spectra for the samples irradiated with increasing nitrogen fluence.

For the lowest nitrogen fluence of 0.6×10^{17} ions/cm^2, the CEMS analysis showed the presence of α-Fe, with a hyperfine field of 33.0 T. The relative contribution to the spectrum corresponding to this phase was 32.6%. Also, the nitride ε-Fe$_{2+x}$N phase was identified, with a relative abundance of 51%. A nitride paramagnetic phase, which cannot be precisely identified, was also found. These unresolved nitride phases gave a 15.5% relative contribution to the CEM spectra.

In the sample, which was irradiated to a fluence of 1.0×10^{17} ions/cm^2, the CEMS analysis showed one singlet, one doublet and five sextets. The relative abundances of the α-Fe and ε-Fe$_{2+x}$N phases slightly decreased, from 32.6 % to 26% and from 51 % to 49%, respectively. The origin of a broad sextet, with a hyperfine field of 29.4 T and an IS of –0.039 mm/s does not provide any clear information about the nitride phase it originates from: is it the α'-FeN or the γ'-Fe$_4$N phase, or both of them? One additional doublet with a 14% fraction indicates the possible presence of the unresolved nitride phase.

36
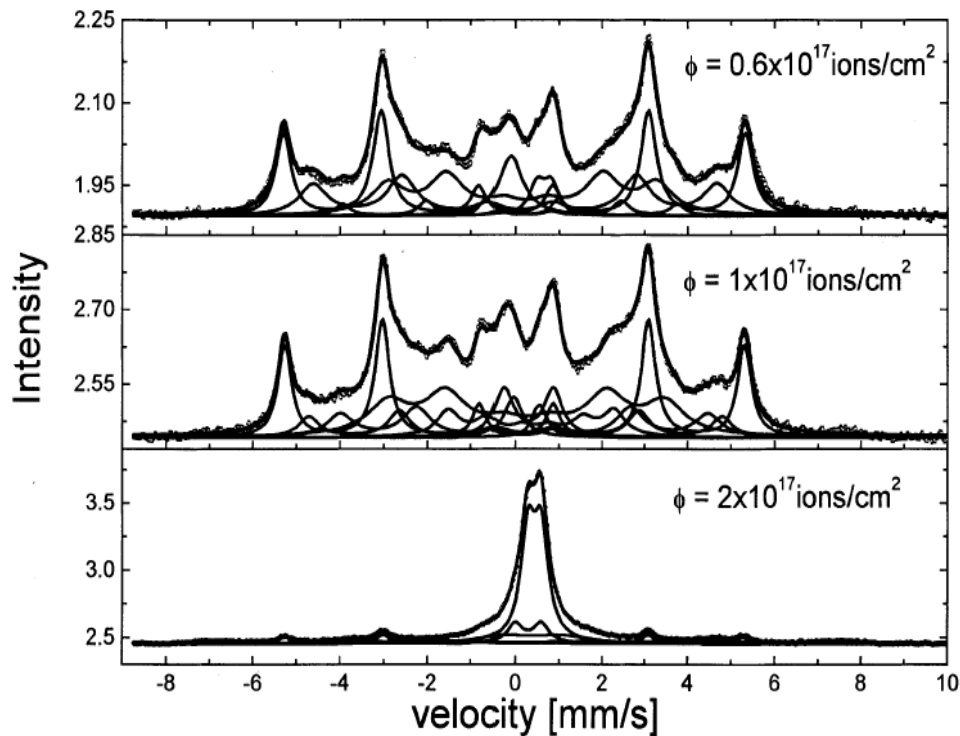
Figure 4.2.3 CEMS measurements of a ^{57}Fe/Si bilayers irradiated with 22 keV N^{++} ions to 0.6×10^{17}, 1.0×10^{17} and 2.0×10^{17} ions/cm^2.

Finally, the CEM spectra of the sample irradiated at the highest fluence of 2.0×10^{17} ions/cm^2 was successfully fitted with two doublets and four sextets. Two doublets were assigned to the ε-Fe$_2$N phase, with a relative abundance of 61%. One sextet with a relative abundance of 7.6%, and a hyperfine field of 33.0 T, was assigned to α-Fe. The remaining sextets, with a relative abundance of 19%, were assigned to a mixture of the α'-FeN and γ'-Fe$_4$N phases.

The evolution of the phase transitions derived from CEMS analyses is summarized in Figure 4.2.4. This figure shows that the fraction of the α-Fe phase decreased with increasing nitrogen fluence. A complete transformation of α-Fe into nitrides is not achieved, not even for the highest fluence. However, the abundance of this phase (7.6 %) is considerably lower than the one obtained when implanting nitrogen into bulk iron (20%) [4-9]. This significant difference can be attributed to the high concentration of defects in the thin film, which develop during the deposition process. These additional defects contribute to the enhanced reaction of iron and nitrogen and in this way the higher relative fractions of nitrides are achieved.
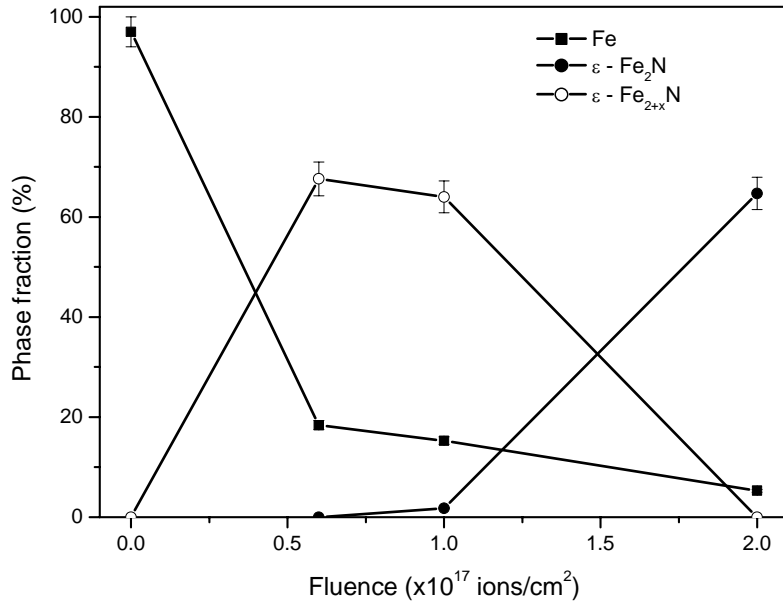
Figure 4.2.4 Nitride phase fractions as observed by CEMS as a function of the ion fluence Φ. The ^{57}Fe(30 nm)/Si samples were irradiated at room temperature with 22 keV ^{14}N^{2+} ions.

The relative fraction of ε-Fe$_{2+x}$N is almost constant after irradiation at low fluences. In the sample irradiated with the highest nitrogen fluence, the nitrogen richer ε-Fe$_2$N phase appears with a rather large fraction of 61%, while the iron-rich nitride phase ε-Fe$_{2+x}$N almost disappears. According to CEM measurements, as in the case of XRD measurements, iron silicides are not observed in the samples. In conclusion, high-fluence nitrogen irradiation of Fe(30nm)/Si bilayers finally produces the ε-Fe$_2$N nitride, but neither iron-silicide nor silicon nitride [4-10].

4.2.2. Ion beam mixing

According to the procedure discussed in Chapter 2, the interface variance σ^2 of the Fe/Si mixed region was deduced from the Fe and Si depth profiles as a function of the ion fluence Φ. An average atomic density of Fe and Si of 67.3 at/nm^3 was used to convert the depth scale into nm. From the slope of $\Delta\sigma^2(\Phi)$ (see Fig 4.2.5) a mixing rate of k = $\Delta\sigma^2$ / Φ = 0.55 (12) nm^4 was determined.

Neglecting the chemical effects that can be caused by nitrogen ions, the atomic transport across the Fe/Si interface is expected to be dominated by ballistic effects [4-11,12]. The expression for the ballistic mixing k$_{ball}$ (Chapter 2.1.3, Eq 2.10) is:

$$\Delta\sigma^2/\Phi = k_{\text{ball}} = \frac{1}{3}\Gamma_0\xi\frac{R_d^2}{NE_d}F_D \, ,$$

where $\Gamma_0 = 0.608$, ξ is a kinematic factor involving the masses of the colliding target atoms, N the average atomic density, $R_d \approx 1$ nm the minimum separation distance for the production of a stable Frenkel pair, E_d (≈ 20 eV) the average displacement energy, and $F_D = 0.18$ keV/nm the average energy density deposited at the interface, and it gives $k_{\text{ball}} \sim 0.03$ nm^4. It is clear that the experimental mixing rate is at least by one order of magnitude larger than the mixing rate estimated by the ballistic mixing model. This result is in contrast to the experiments performed with Xe ions irradiating strongly bound nitride (AlN or TiN)/metal bilayers [4-13], where the ballistic mixing model proved to be very successful. For Xe ion irradiation of the weakly bound nitride Ni$_3$N on an Al or Si substrate, the thermal spike mixing model was successful [4-1,14]. In our case, the absence of any silicide phase excludes thermal spike mixing at the Fe/Si interface.
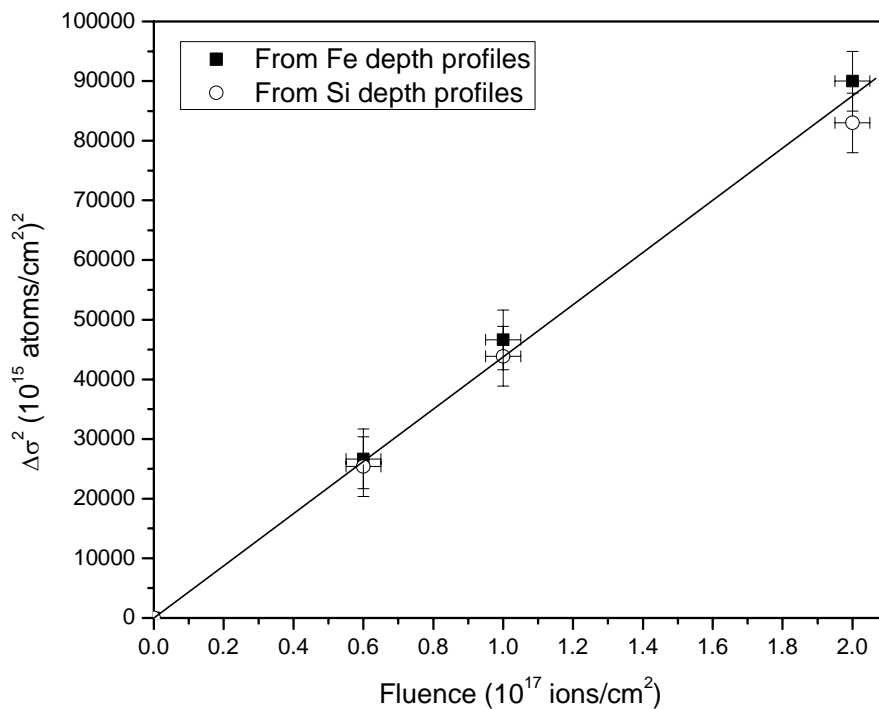
Figure 4.2.5 Interface broadening variance $\Delta\sigma^2(\Phi)$ versus ion fluence Φ in Fe/Si bilayers irradiated with 22 keV N^{++}.

4.3. Annealing: results and discussion

The sample irradiated at a fluence of 1×10^{17} ions/cm^2 was chosen for a post - annealing treatment. The sample was annealed in vacuum at a pressure below 2×10^{-6} mbar between 100°C and 700°C. Each annealing step took one hour. After each annealing process, RBS, XRD, and CEMS measurements were performed [4-15]. In Figure 4.3.1, the Si and Fe depth profiles obtained by RBS at various annealing temperatures are shown.
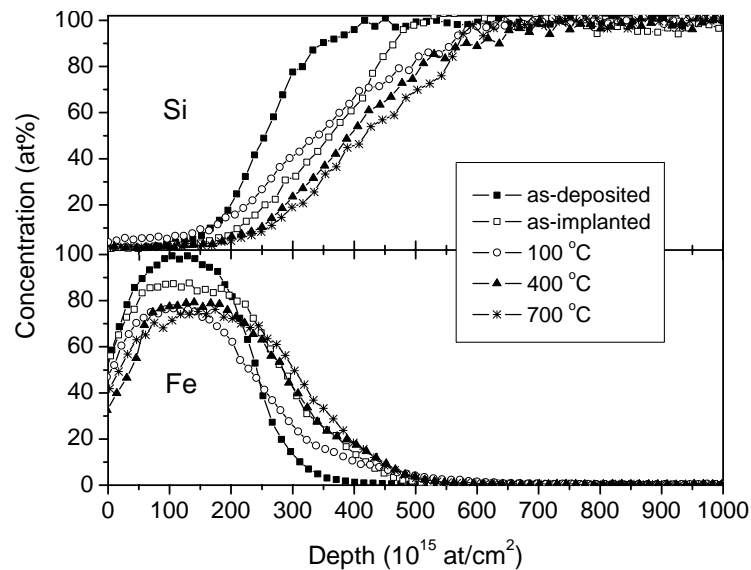
Figure 4.3.1 Selected depth profiles obtained from the RBS spectra taken after post-annealing the sample irradiated to a fluence of 1×10^{17} ions/cm^2 for 1 h at the given temperatures.

After nitrogen irradiation, the Fe concentration decreases from 100 at. % to about 85 at. %. As a result of the post – annealing treatment, the maximum Fe concentration decreases further to about 75 at. % and almost stays constant during all subsequent thermal annealing steps (up to 700 ^{o}C). In contrast to this behavior of the maximum concentration of iron, the broadening of the Fe/Si interface becomes more and more pronounced when increasing the annealing temperature. The overlapping of the Fe and Si depth profiles indicates that Fe and Si migrate towards each other, and possibly form iron-silicides. However, due to the fact that there is no region with constant Fe and Si concentrations, not a single silicide phase was formed.
The influence of the thermal post-annealing treatment, viewed by XRD, is presented in Fig. 4.3.2. All the scans were performed in glancing-incidence geometry with X-ray angle fixed to 3°.
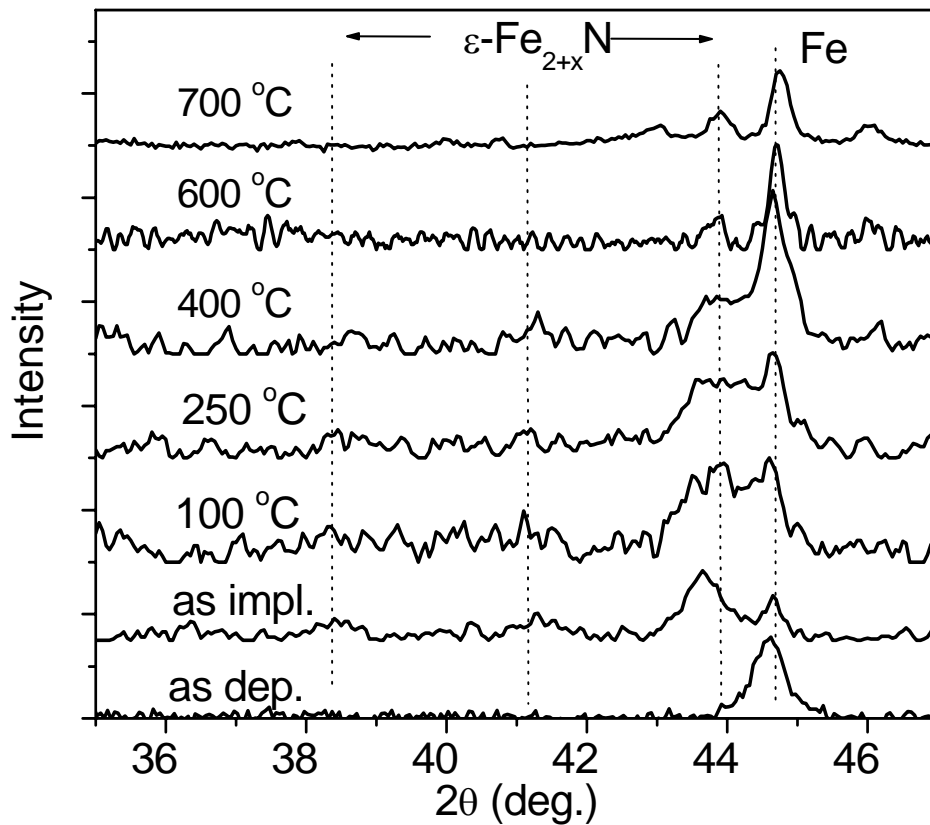
Figure 4.3.2 XRD spectra of the successively annealed sample irradiated to a fluence of 1×10^{17} ions/cm^2 .

The small thickness of the Fe layer of only 30 nm did not provide satisfactory counting statistics; consequently, the information obtained from the XRD spectra was insufficient. Besides the peak that corresponds to the iron, we only observed those of ε-Fe$_{2+x}$N up to 400 ^{o}C. Slight changes in the position of the main peak of this phase suggest a variation of the nitrogen content.
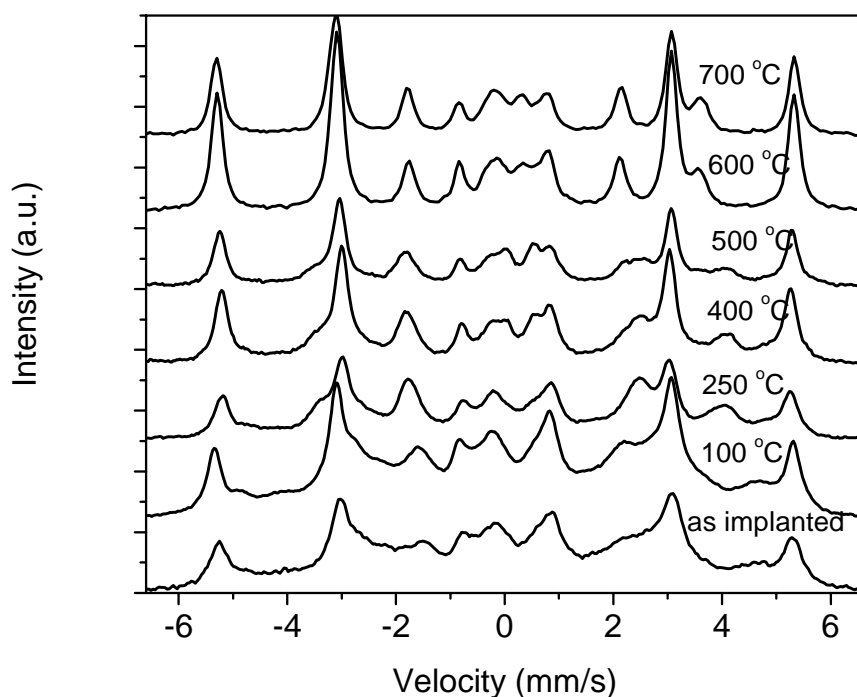
Figure 4.3.3 CEM spectra of the successively annealed ^{57}Fe/Si bilayer.

The most comprehensive information was gained by the CEMS measurements. Fig. 4.3.3 shows the CEM spectra after each thermal annealing step. In all these cases we identified a sextet with a hyperfine field of $B_{hf} = 33$ T and a vanishing isomer shift δ and a quadrupole splitting QS that corresponds to α-Fe. We also identified 2-3 additional sextets with fields of $B_{hf} = 7.0$ T to 29.8 T corresponding to the ε-Fe$_{2+x}$N phase. As the hyperfine field linearly depends on the nitrogen content [4-16], it can also be used to determine the nitrogen concentration in this phase. The three more further sextets with $B_{hf} = 21.55(4)$ T, 21.92(4) T and 34.06(5) T correspond to the γ'-Fe$_4$N phase [4-17]. Two doublets describe the silicide phase β-FeSi$_2$ with isomer shifts of 0.09(1) mm/s and 0.10(1) mm/s and quadrupole splittings of 0.54(2) mm/s and 0.32(1) mm/s, respectively [4-18]. Values of 0.80 (α-Fe), 0.35 (ε-Fe$_3$N), 0.55 (γ'-Fe$_4$N) and 0.90 (β-FeSi$_2$) were used as Debye-Waller factors. One example of the deconvolution of the CEM spectra is shown in Chapter 3. In Fig. 4.3.4, the deduced phase fractions are plotted as a function of the annealing temperature. The predominant phase, up to an annealing temperature of 400$^{\rm o}$C, is iron-rich ε-Fe$_{2+x}$N; its fraction is 75 % at 250$^{\rm o}$C. This phase fraction starts to decrease at 400$^{\rm o}$C and is below the detection limit at 600$^{\rm o}$C. After annealing at 400$^{\rm o}$C, the phase γ'-Fe$_4$N appears, whose abundance reaches 50 % after the last annealing step at 700$^{\rm o}$C. Between 100$^{\rm o}$C

and 500°C we observed a small amount ($\approx 5\%$) of amorphous iron-silicide. This fraction may have been underestimated because of its unknown Debye-Waller factor. Only after annealing at 600°C and 700°C annealing the β-FeSi$_2$ iron silicide phase was observed, with a fraction of about 10%.
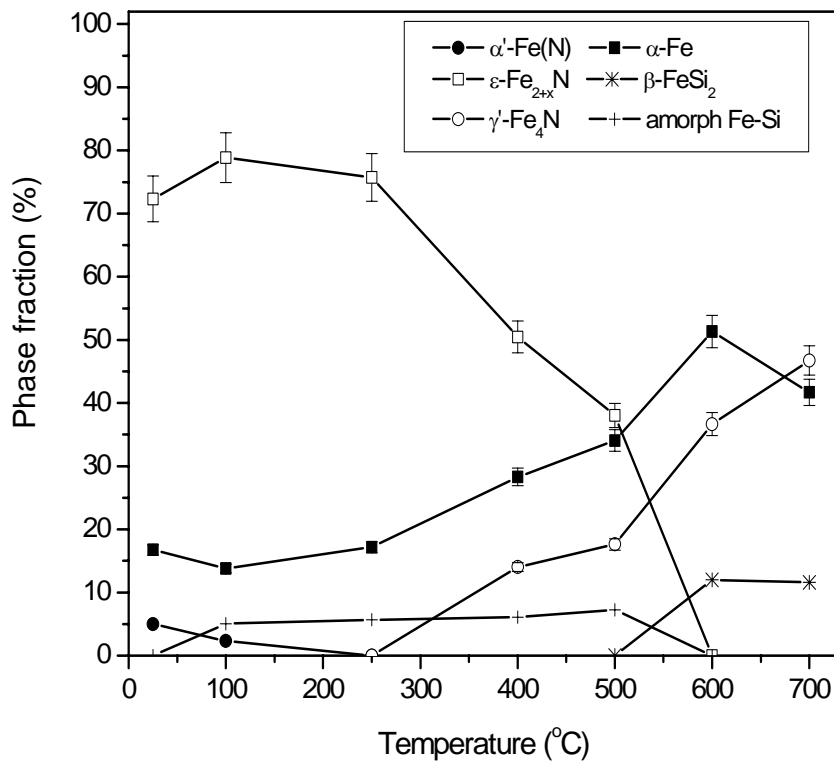
Figure 4.3.4 Phase fractions of various iron-nitrides and iron-silicidies observed by CEMS as a function of the annealing temperature.

The relative nitrogen content in the sample bound to iron, c_{N-Fe}, was calculated from the measured iron nitride phase fractions. As shown in Fig. 4.3.5 this quantity decreases rapidly after the annealing at 250°C and continues to decrease up to 600°C. At this temperature region, the formation of iron-silicides occurs at the Fe/Si interface and at the same time nitride decomposition starts, followed by nitrogen outdiffusion.
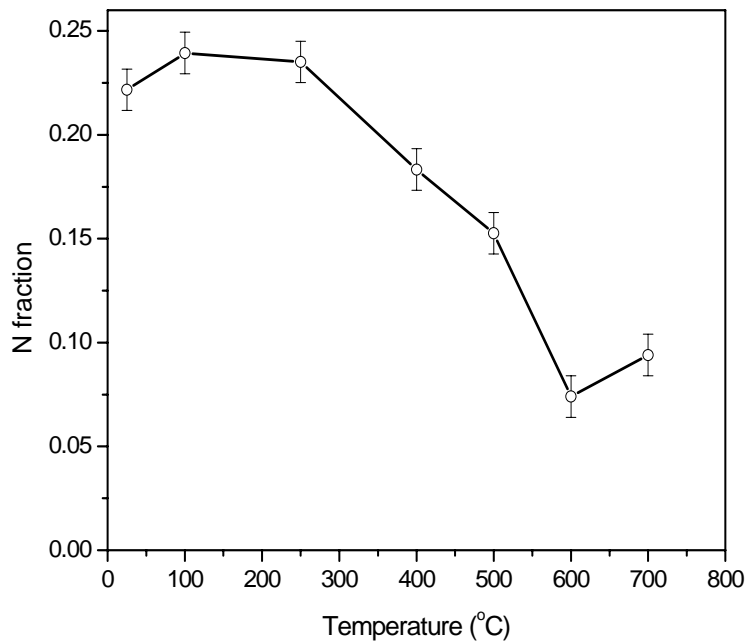
Figure 4.3.5 Total relative nitrogen content bound to iron and observed by CEMS.

5. Effects of substrate amorphization and ion charge

5.1. Sample preparation

In these sets of experiments two types of samples were prepared: with and without amorphization of the Si substrate prior to iron deposition. These two different types of bilayers were labeled as Fe/aSi and Fe/Si. Amorphization was performed with a 1.0 keV Ar^+ ion beam. The projected range of 1.0 keV Ar^+ ions and the sputtering yield are 3.5 (16) nm and 0.8(3) atoms/ion, respectively [5-1]; so all the changes in the Si substrate are located near the surface of the wafer. Fig. 5.1 shows a scanning electron microscope (SEM) picture of the amorphized sample (aSi), which clearly shows that no additional roughening was induced. Two distinct hillocks are attributed to impurities.
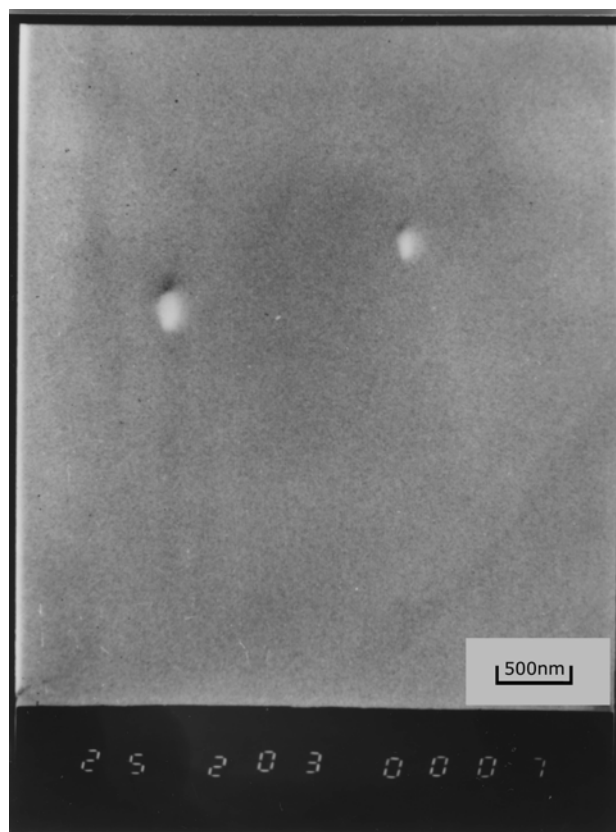
Figure 5.1 SEM picture of the amorphized (aSi) sample: no roughening of the
Si surface due to 1.0 keV Ar^+ beam irradiation.

Surface roughness can cause significant changes to the values of $\Delta\sigma^2$, but this effect was neglected in all these cases as the surface roughness did not change significantly (less than 2 nm). From the SEM figure shown in Fig.5.1, any possible roughening of the Si wafer surface due to the 1.0 keV Ar irradiation is well beyond the detection limit.

Iron layers of 30-40 nm thickness were deposited by e-beam evaporation at a rate of 0.5 nm/s and a base pressure of 10^{-7} mbar [5-2]. Irradiations of the samples were performed at room temperature with different types of noble gas-ions and different charge states, namely: Ar^{1+} and Ar^{8+}, Kr^{1+} and Kr^{11+}, Xe^{1+} and Xe^{17+}. The energies of the ions were chosen in such a way that the deposited energy per ion and unit length (F_D) had its maximum at the iron-silicon interface. Energies of 100 keV were used for argon ions, 180 keV for krypton, and 250 keV for xenon. In this energy range of the ions and thickness of the top iron layer, nuclear energy loss is dominant in the Fe-Si interface region (Chapter 2.1.1, Fig. 2.3). Irradiation experiments with singly-charged ions were performed with the IONAS implanter in Goettingen [5-3], while irradiations with the multiply charged ions were carried out at the TESLA facility at Vinca [5-2]. The experimental mixing rates were obtained by means of RBS, using a 900 keV He^{2+} beam of the IONAS accelerator; the spectra were analyzed by means of the WiNDF code [5-4].

5.2. Results and discussion

Numerous experiments and analyses were done in the scope of this topic. As an example, RBS spectra, the deduced depth profiles and the interface variance $\Delta\sigma^2$ versus the fluence Φ of the 32 nm thick iron layer on an amorphized Si wafer (aSi), irradiated with 250 keV Xe^{1+} and different fluences are shown in Figures 5.2 and 5.3. The transformation from "natural RBS depth units" (at/cm^2) to "normal depth units" (nm) was performed by using the average atomic density of iron and silicon at the interface: $\rho_{ave} = 67.3$ at./nm^3.
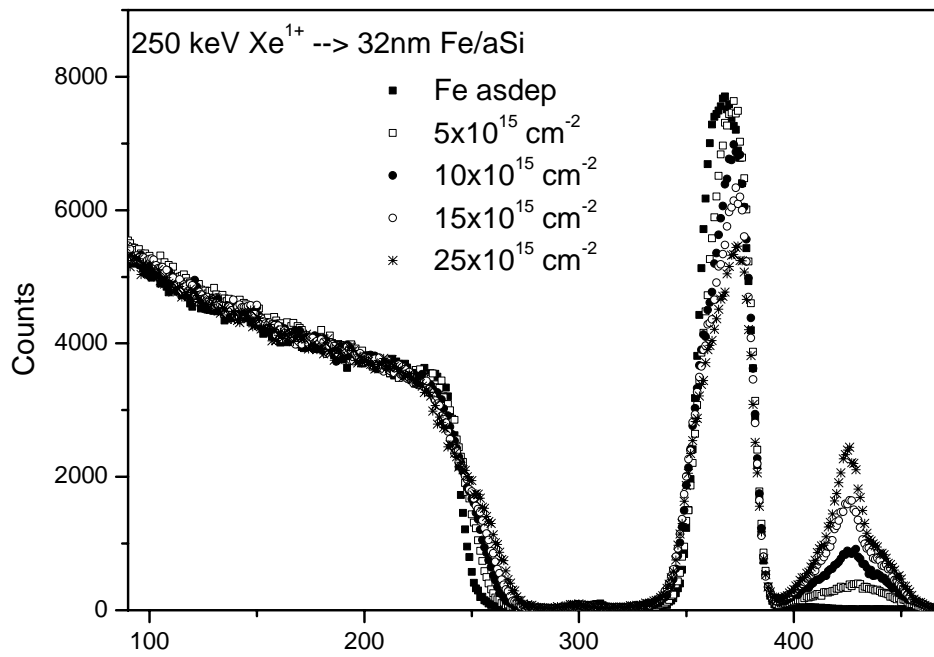
Figure 5.2 Raw RBS spectra of a 32 nm thick iron layer on an amorphized Si wafer (aSi), irradiated with 250 keV Xe^{1+} to a different fluences.
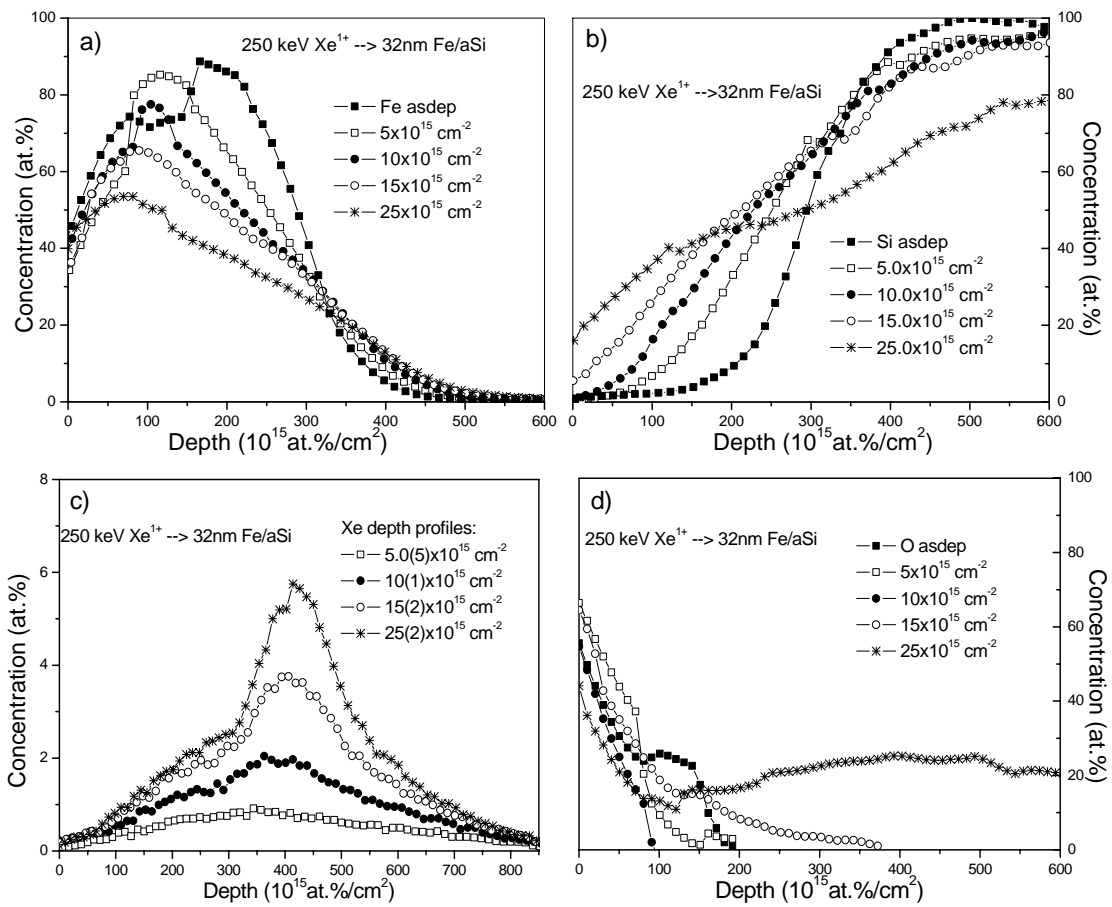

Figure 5.3 Obtained depth profiles of iron (a), silicon (b), xenon (c) and oxygen (d): results of the fitting procedure of the raw RBS spectra shown in Fig 5.2.

By the integration of the Fe depth profiles (Fig. 5.3a), and a comparison of the irradiated and the as-deposited samples, the experimental sputtering yield was found to be 3.6(6) atoms/ion. Consequently, there was a slight decrease in the iron layer, about 5 nm for the fluence of 15×10^{15} Xe/cm^2. The influence of the sputtering effect can also be noticed at the Si depth profiles: with increasing fluence the silicon edge is shifted toward the top of the sample. Xenon was the heaviest ion used in these sets of experiments, and the sputtering effect was less pronounced in the case of irradiations with argon and krypton ions.

A changes in the variance σ^2 of the silicon depth profiles (Fig. 5.3b), as a function of the ion fluence, provides the slope of the linear curve (Fig 5.4), which is the mixing rate $\Delta\sigma^2/\Phi$. The data for the highest fluence were not taken into account in the calculation of the mixing rate. In this case, the Fe-Si interface is heavily contaminated with oxygen during irradiation (see Fig.5.3d) and it represents a different system. The exact ion fluence was obtained by the integration of the Xe depth profiles (Fig.5.3c)
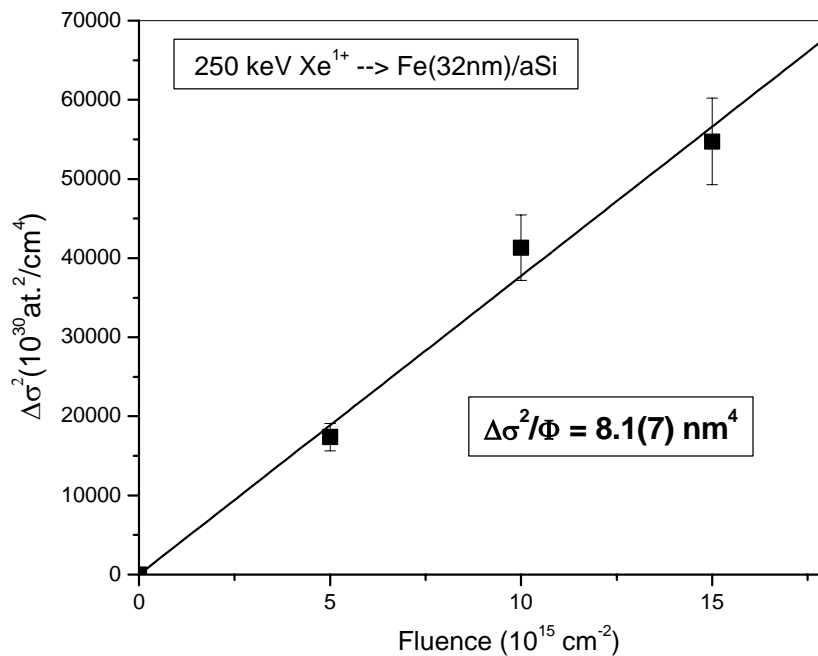
Figure 5.4 Interface variance of the mixed Fe/Si interface $\Delta\sigma^2$ as function of the Xe ion fluence Φ. Also slope of the linear curve is indicated $\Delta\sigma^2/\Phi$, labeled as mixing rate.

Fig. 5.5 shows the ion ranges and the deposited energy per ion per unit length, F_D. These results were obtained using the SRIM code.
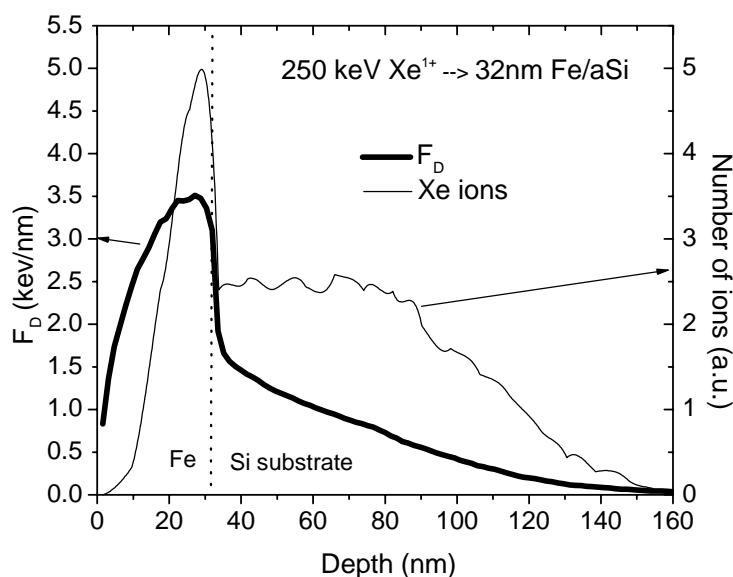
Figure 5.5 Xe implantation distribution and deposited energy per ion per unit length, F_D, calculated by means of the SRIM code.

As can be seen in Fig. 5.5, most Xe ions rested in the Si substrate, but their energy was chosen in such a way that the deposited energy reaches its maximum at the Fe - aSi interface. The deposited energy is slightly changed with increasing ion fluence, due to the sputtering effect; however, this effect was not taken into account. Equivalent calculations were performed in all these cases, and the deduced mixing rates are summarized in Table 5.1.

Table 5.1 Summary of the irradiation experiments with singly and multiple charged ions of samples with amorphized and non-amorphized Si substrates before iron deposition, as well as comparison with different ion beam mixing models.

Ion energy (keV)	Ion	Mixing rate $\Delta\sigma^2/\Phi$ (nm^4)					F_D (keV/nm)
		Experimental, for two types of substrates		Model			
		Fe/aSi	Fe/Si	Ball	Local	Global	
100	Ar^{1+}	2.7(3)	1.5(2)[*]	0.18	1.4	0.5	1.0
	Ar^{8+}	3.3(5)	2.1(2)[*]				
180	Kr^{1+}	4.0(3)	2.6(2)	0.28	2.9	2.0	2.0
	Kr^{11+}	4.3(9)	2.7(5)				
250	Xe^{1+}	8.1(7)	4.8(5)[*]	0.5	4.0	3.5	2.8
	Xe^{17+}	9.3(6)	4.5(5)				

[*]-Ref.: [5-5]

Each of the experimental mixing rates shown in Table 5.1 was obtained by analyzing five RBS spectra for the four different fluences of each ion and for the as-deposited samples. In all the cases $\Delta\sigma^2$ varied linearly with the fluence and the well-defined slopes $\Delta\sigma^2/\Phi$ were obtained. The fluences were in the range between 1 and 28×10^{15} ions/cm^2. The mixing rate values labeled with [*] were taken from Ref. [5-5].

The experimental results, presented in Table 5.1 are shown in the next Figure 5.6.
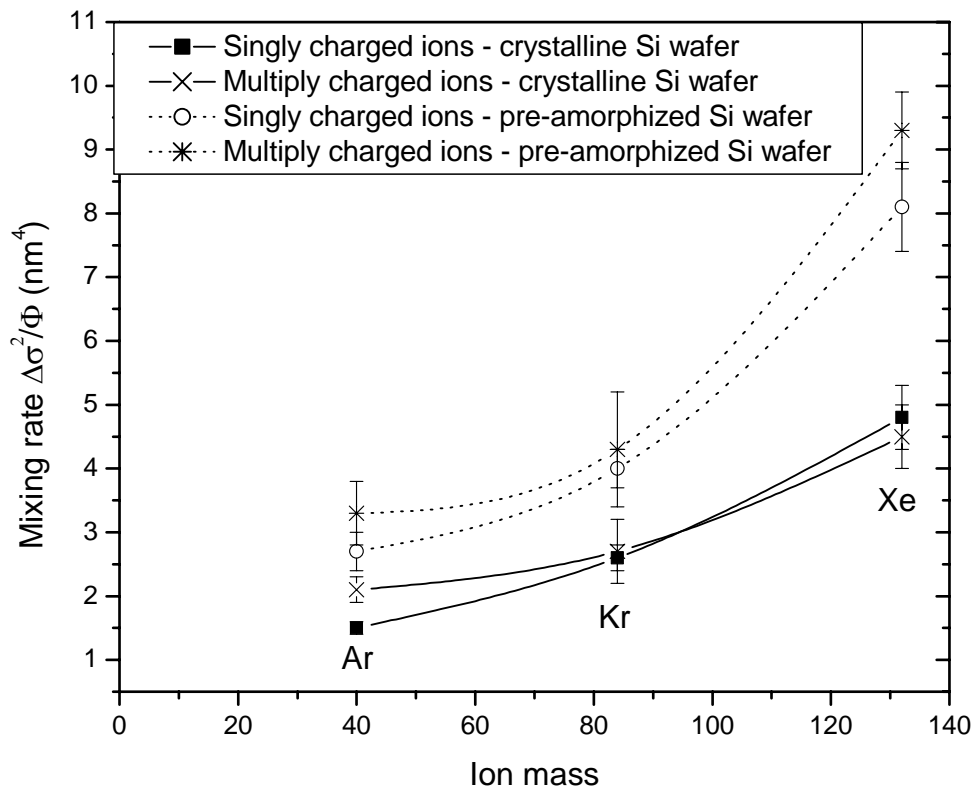
Figure 5.6 Comparison of the mixing rates for singly/multiply charged ions of Ar$^+$/Ar^{8+}, Kr$^+$/Kr^{11+} and Xe$^+$/Xe^{11+} on crystalline and pre-amorphized Si wafers before iron deposition.

The most obvious conclusion is that the mixing rate increases with increasing ion mass and deposited energy F_D. This result was expected and is a well-known effect. However, this large amount of data allows us to draw some more interesting conclusions:

a) Effects of the ion charge

To clarify the influence of the ion charge on the mixing rate, an extensive set of experiments was carried out on the Fe/Si bilayers. Irradiations with three different noble-gas ions were performed: Ar, Kr and Xe; with singly-charge and multiply-charge ion states. For each pair of singly and multiply-charged ion state irradiations, thickness of the top iron layer was the same. Also, both types of Si wafers were used: amorphized and non-amorphized (crystalline). In the case of the Ar^{1+}/Ar^{8+} irradiations, the thickness of the iron layer in the Fe/aSi bilayer was 30 nm. For irradiations with Kr^{1+}/Kr^{11+} and Xe^{1+}/Xe^{17+} the thickness of the top iron layer in Fe/aSi and Fe/Si bilayer systems was 32 nm.

After a careful calculation of the mixing rates, the values listed in Table 5.1 and also shown in Fig 5.6 were obtained. We found out that, in the chosen range of energies and thicknesses , the ion charge state does not have any influence on the mixing rates. The mixing effect was the same for each ion pair, within error bars.

The investigation of the mixing rate as a function of the ion charge state was triggered by the previously published results in Ref. [5-5]. It was reported that the mixing rate in Fe/Si bilayers, due to irradiation with 100 keV Ar^{8+} ions, is about 50% larger than the one obtained by irradiation of the same system with 100 keV Ar^{1+} (Table 5.1). This result was quite surprising, and it is in discrepancy with the mixing rates of Ta/Si bilayers irradiated with 250 keV Xe^{1+} and Xe^{19+} ions. In this case the mixing rates were the same ($\Delta\sigma^2/\Phi=3.5(4)$, Ref. [5-5]). It is known that the ions reach their equilibrium charge state after penetrating of 5-7 nm of the conductive solid matter [5-6], and the thicknesses of the Fe/Si system were in the 30-40 nm range. The sputtering yield in the case of 100 keV Ar ions is negligible, and hence there are no changes in the thickness of the top Fe layer and the deposited energy density. The obviously different behavior of the mixing rates obtained for the $Ar^{1+}/Ar^{8+} \rightarrow$ Fe/Si and $Xe^{1+}/Xe^{19+} \rightarrow$ Ta/Si irradiations was explained with the help of the projected range of the ions. In the case of irradiations with argon, 70% of all ions cross the Fe-Si interface region and are stopped in the Si substrate. In the case of xenon irradiation, only 30% of the ions manage to cross the Ta-Si interface. It was suggested that the probability that some of the Ar ions with higher charge states are able to cross the interface is larger than in the case of the Xe ions and, consequently, the mixing rates

are different for Ar^{1+} and Ar^{8+} irradiations, and they are the same for Xe^{1+} and Xe^{19+} irradiations.

This argumentation was not so convincing. The difference in the charge states of the xenon ions is more than twice as high as the difference between the charge states of the argon ions. If this parameter plays a major role, it would be easier to observe an effect of the charge state in the case of Xe^{1+}/Xe^{19+}. On the other hand, two different systems were compared: Fe/Si and Ta/Si. This effect was observed only in the Fe/Si bilayer. The Fe/Si bilayer system might be especially sensitive to the charge state of ion. Also, the thicknesses of the Fe/Si bilayers were not identical and this may be the reason for the different values of the mixing rates.

The presented results ruled out speculations about the influence of the projected range of the ions and some possible special features of the Fe-Si bilayer system.

b) *Effects of the amorphization of the Si substrate prior to the deposition of the iron layer*

The obtained mixing rates for this part of the experiment are listed in Table 5.1 and plotted in Fig. 5.6. It is clear that in all the cases preamorphization of the Si substrate leads to higher mixing rates, by a factor of 1.8(2) than those of the crystalline Si substrate. The influence of roughening was not considered because the SEM picture (Fig. 5.1) did not show any significant roughening of the surface of the Si wafer. RBS measurements led to the same result. Figure 5.6 shows the Si depth profiles of the Fe/aSi and Fe/Si as-deposited samples. RBS is not able to resolve any roughening of the bulk systems, but can supply this information with respect to the interfaces. When alpha particles hit the surface of the bulk material, they will collide with surface atoms with the same energy, regardless of the relative position of the surface atoms to each other. Consequently, the backscattered alpha particles will have the same energy, and the counts will be collected around the same channel, spread by the resolution of the RBS system. When RBS measurements are performed with the bilayer system, due to the different thicknesses of the top layer, introduced by the roughens, the alpha particles will loose different amounts of energy before they hit the substrate layer. Thus the backscattered particles will have slightly different energies, and any spreading of the substrate signal will be larger than for ideal flat surfaces. The spreading of the signal is not only caused by the roughness of the substrate, but also

by the roughness of the surface of the top layer. In Fig. 5.7 the same slopes of the silicon depth profiles of Fe/aSi and Fe/Si as-deposited bilayers can be seen. The difference between the Si depth profiles of two types of Fe-Si bilayers, pre-amorhized and crystalline Si wafers, is 1 nm, (using the average atomic density of iron and silicon at the interface: ρ_{ave}= 67.3 at./nm^3). The spreading is caused only by the resolution of the RBS system used. So, within 1 nm, according to the RBS analysis, interface and surface of the two types of bilayers, Fe/aSi and Fe/Si, can be considered to be flat.
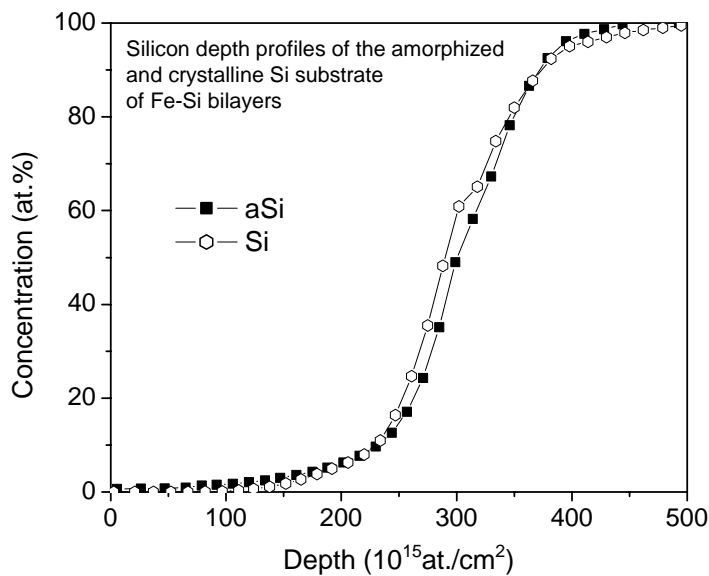
Figure 5.7 Si depth profiles of the Fe/aSi and Fe/Si as-deposited samples.

The only remaining effect of the treatment of the Si substrate with a low-energy Ar$^+$ beam prior to the deposition of an iron layer is amorphization. Argon ions break the crystal lattice of the silicon, thus the Si atoms are more mobile and can easily diffuse in to the iron layer during the irradiation process. Their mobility is almost doubled, which is shown by the larger mixing rate.

c) A comparison of experimental and model mixing rates

It is obvious (see Table 5.1) that ballistic mixing (Chapter 2.1a) underestimates the experimental mixing rates by one order of magnitude, as expected for heavy-on bilayer-systems. Either local or global spikes can explain the results for the

experimental mixing rates. The local spike mixing model (Chapter 2.1b) reproduces the mixing rates in the mixing experiments with the Fe/Si system very well. On the other hand, the global spike mixing model (Chapter 2.1c) is less successful in all the cases. This model supplies the best prediction for irradiation experiments with Xe ions. Here the highest value of the deposited energy, F_D, is 2.8 keV/nm. In our set of experiments, the transition between local and global spikes appears to occur at a deposited energy density higher than 2.8 keV/nm.

For higher mixing rates obtained in the experiments with Fe/aSi bilayers, none of the models is suitable and modifications of the mixing models are necessary.

6. Swift ion irradiation with 350 MeV Au ions

In contrast to the experiments described previously, where the nuclear stopping of the ions played an important role, in this set of experiments nuclear stopping is negligible and electronic stopping is predominant. At those chosen energy of 350 MeV Au ions it is possible to investigate interface mixing and phase formation in the regime of pure electronic stopping.

6.1. Sample preparation

Two sets of samples were prepared for the swift heavy ion irradiation experiments: ^{nat}Fe(50 nm)/Si bilayers and ^{nat}Fe(45 nm)/^{57}Fe (20 nm)/Si trilayers.

The ^{nat}Fe(50 nm)/Si bilayers were prepared in a UHV chamber [6-1] by electron-beam evaporation of the iron. The deposition rate was about 0.5 nm/s, and the base pressure in the chamber was below $4 \cdot 10^{-8}$ mbar.

The trilayer films of ^{nat}Fe(45 nm)/^{57}Fe (20 nm)/Si were deposited at room temperature by pulsed laser deposition. The ambient pressure in the deposition chamber was below 10^{-8} mbar. These samples, with a ^{57}Fe sandwiched layer, were used for extensive CEMS and MOMS measurements. They were prepared at the Leibniz Institut für Festkörper und Werkstoffforschung (IFW), Dresden.

The samples were homogeneously irradiated across a 7×7 mm area with 350 MeV Au^{26+} ions and a 100 nA beam at the ECR-RFQ cyclotron accelerator facility of the Hahn-Meiter-Institut, Berlin [6-2] at fluences of up to 5×10^{15} ions/cm^2. The irradiations were performed either at room temperature or at 92 K. In all the cases the ambient pressure during irradiation process was below 10^{-6} mbar.

6.2. Results and discussion

SRIM simulations [6-3] of the irradiation of ^{nat}Fe(45 nm)/^{57}Fe (20 nm)/Si trilayers with 350 MeV Au^{26+} ions suggest that the nuclear stopping power in the iron layers and in the Si substrate near the interface are: $S_n(Si) = 23$ eV/nm and $S_n(Fe) = 90$ eV/nm. The electronic stopping is by three orders of magnitude higher and its values

are: $S_e(Si) = 19$ keV/nm and $S_e(Fe) = 52$ keV/nm. The nuclear and electronic stopping powers are almost constant in the upper 200 nm of the samples (Fig. 6.2.1.). The projected range of the Au ions is deeply in the Si substrate, and it is about 27 nm.
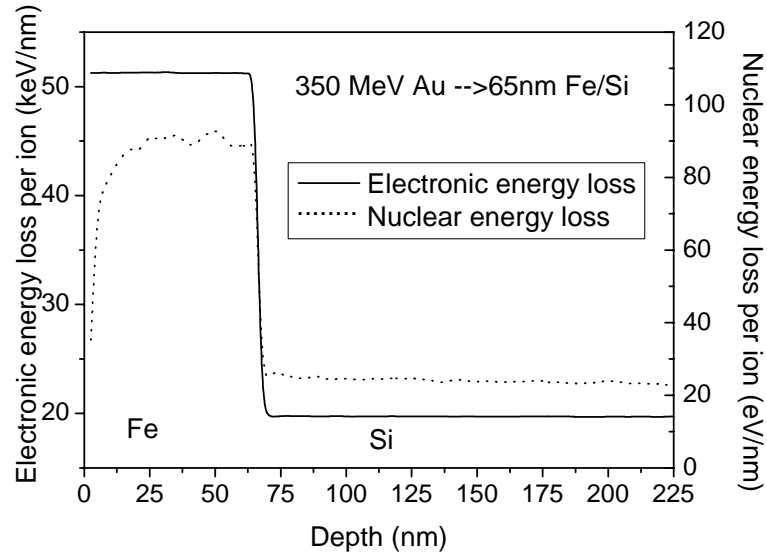

Figure 6.2.1 SRIM simulations of the irradiation of Fe(65 nm)/Si trilayers with 350 MeV Au ions.
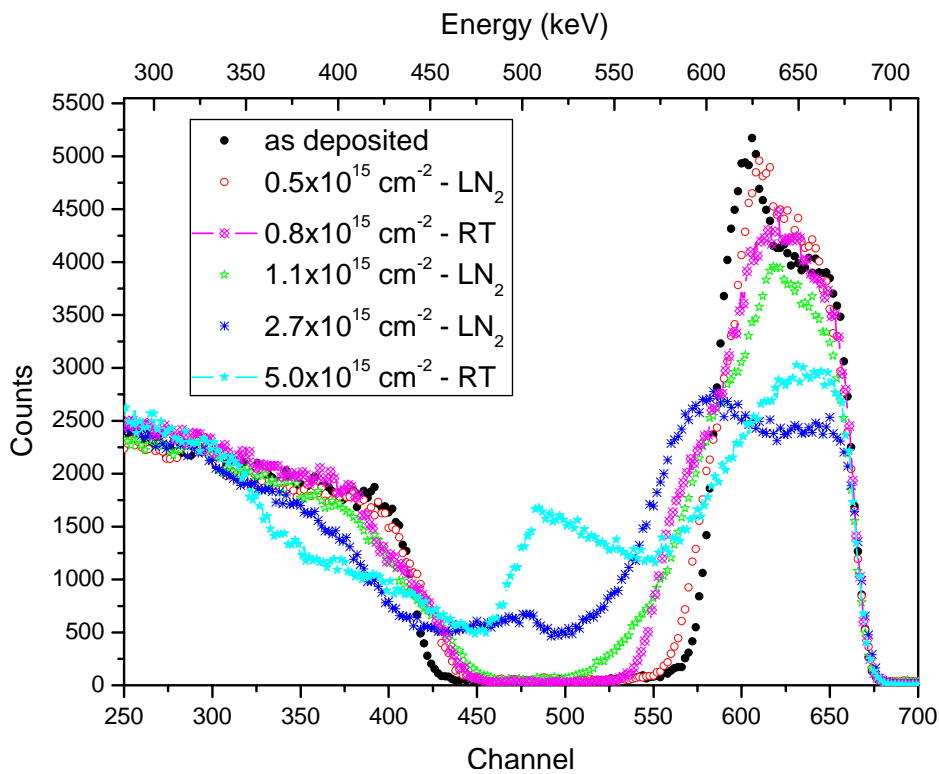

Fig 6.2.2 Selected raw RBS spectra measured before and after irradiation of the ^{nat}Fe(45 nm)/^{57}Fe (20 nm)/Si trilayers. The irradiations were performed at different fluences and two temperatures: liquid nitrogen (LN$_2$) and room temperature (RT), as indicated in the picture.

Fig 6.2.2, which represents selected RBS spectra of the trilayer samples, shows that silicon reaches the sample surface when it is irradiated at the highest fluences (2.7×10^{15} and 5.0×10^{15} cm^{-2}), which is indicated by a clear peak at channel 480. For all other fluences the silicon and iron signals were separated. From the measured broadening of the silicon signal (Fig. 6.2.3a) the experimental mixing rate of $\Delta\sigma^2/\Phi =$

(a)   (b)
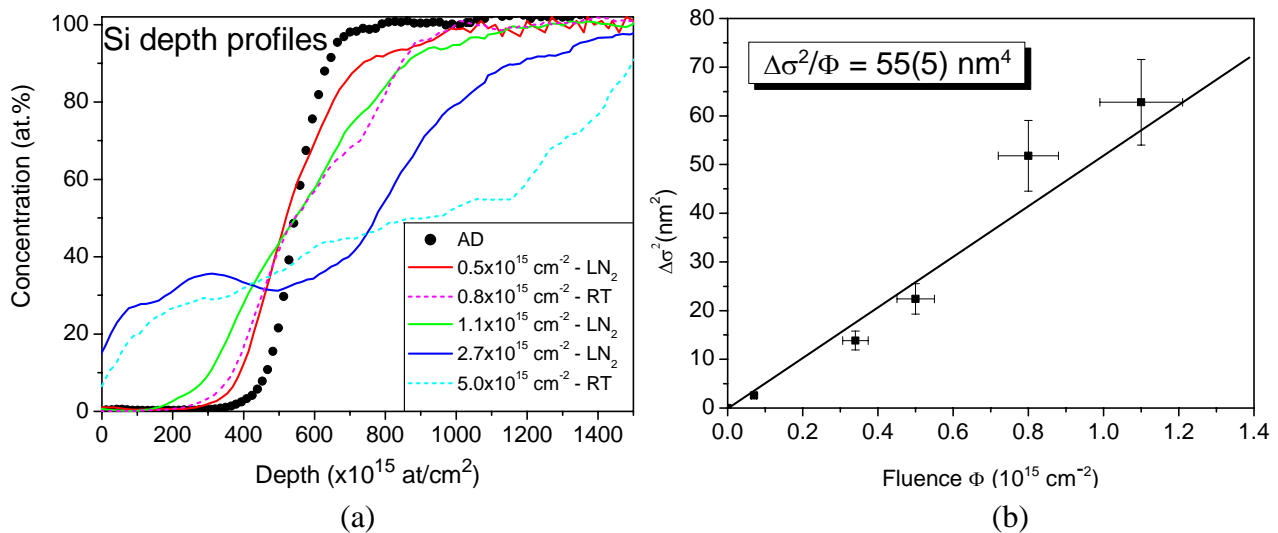
Figure 6.2.3 Broadening of the silicon depth profile (a) and interface variance of the mixed Fe/Si interface $\Delta\sigma^2$ as a function of the Xe ion fluence Φ (b). Also the slope of the linear curve is indicated ($\Delta\sigma^2/\Phi$), labeled as mixing rate.

55(5) nm^4 was calculated (Fig. 6.2.3b).
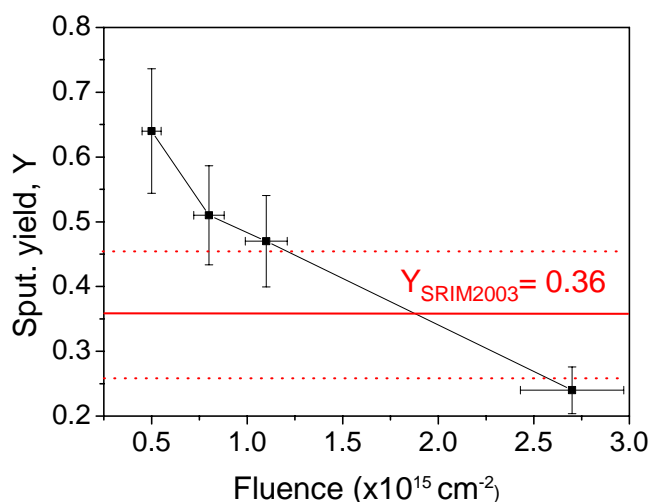
Figure 6.2.4 Calculated sputtering yield for the trilayers irradiated at different fluences, as well as SRIM result.

By integrating the iron depth profiles the sputtering yield, which is close to the SRIM predictions, was deduced. It decreases with increasing ion fluence (Fig 6.2.4), indicating the structural changes in the upper part of the sample, probably iron-oxide formation [6-4] and iron-silicide.

The deduced mixing rate of 55(5) nm^4 is by one order of magnitude higher than the mixing rates measured for the 250 - 700 keV Xe$^+$ or Au$^+$ ions [6-5]. In these experiments, where nuclear stopping plays a major role, the mixing rate of the Fe/Si bilayers was in the range of 5-9 nm^4. The rather big mixing effect of the bilayers when electronic stopping is dominant was explained by a transfer of the energy deposited by the ions in the electronic subsystem to the lattice [6-6,7,8]. It was assumed that the energy deposited initially in the electronic subsystem within 10^{-15} - 10^{-14} s gets transferred to the atomic subsystem by electron-phonon coupling in 10^{-13} - 10^{-12} s. As a result of this transfer, a rapid rise of the lattice temperature up to 10^4 K occurs along the ion path (thermal spike). If a certain threshold of energy loss is exceeded, the material within few nanometers from the ion path melts for a duration of 10^{-12} - 10^{-11} s. The molten region rapidly quenches at a rate of about 10^{-14} K/s, forming latent tracks. It is interesting to note that in order to reach the melting point of Si, the calculated critical value of the energy deposited due to electronic stopping is about 10 keV/nm [6-9, 10]. Experimental proof of this result does not exist yet. The fact that no latent tracks in bulk Si were observed can be attributed to the recrystallization of the molten region.

The electronic energy loss in our experiment is sufficient to produce a molten region in both layers (Fe and Si). In this way, the conditions for forming thermal spikes are fulfilled, and interdiffusion of Fe and Si occurs in the molten region. The large mixing rate of 55(5) nm^4 gave us evidence of this process.

It was reported that a significant diffusion of oxygen occurs during high-energy ion irradiations of iron [6-4]. Bearing this in mind, the decreasing sputtering yield for increasing ion fluence can be explained on the basis of these facts. The formation of a thin top layer of oxide reduces the sputtering yield by a factor of three.

In the RBS measurements no significant difference was observed in the samples irradiated at liquid nitrogen and room temperature.

Further information about irradiated bi/tri-layers was obtained by XRD and CEMS measurements.

The XRD measurements were performed in glancing incidence geometry, with an X-ray source fixed at 3°. The measurements ranged from 17° to 102°, with a step size of 0.1^o (see Fig 6.2.5).
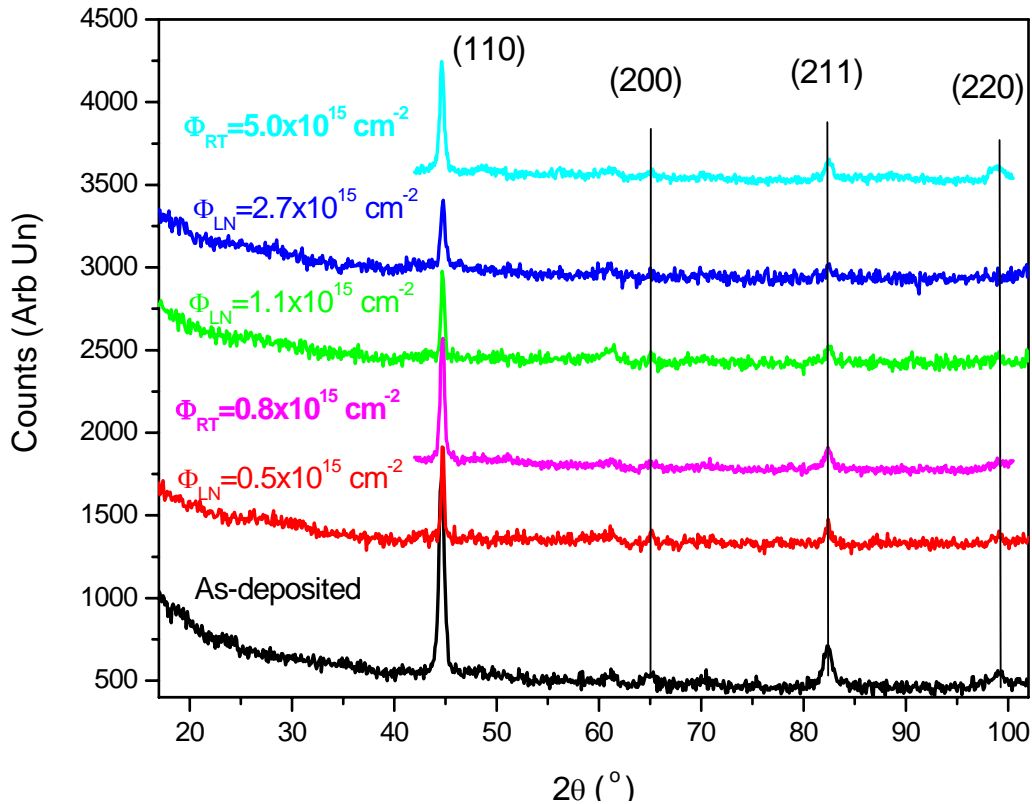
Figure 6.2.5 Glancing incidence XRD measurements of the as-deposited and irradiated samples; different reflections of the iron are indicated.

The XRD scans do not show any crystalline iron silicide phase. In all the samples the peak corresponding to the strongest reflection of iron (110) is present, as well as the (211) reflection. The intensities of both peaks decreased with increasing fluence, indicating a reduction in the crystalline iron phase and the formation of amorphous iron silicide phases.

Fig 6.2.6 shows the CEM spectra of the as-deposited and irradiated samples. Up to a fluence of 1.1×10^{15} cm^{-2} a sextet with a hyperfine field of 33 T can be identified, that corresponds to α-Fe. The intensity of this sextet in the CEM spectra decreased with the ion fluence, and finally disappeared in the spectrum taken of the sample irradiated at 2.7×10^{15} cm^{-2}. There is another sextet with a smaller hyperfine field of 27.7(3) T, which is broad. This indicates that an amorphous ferromagnetic iron-silicon phase has formed. This broad sextet appears after irradiation at the lowest fluence, but disappears after irradiation at the highest fluence, where only two broad doublets with

central shifts of 0.19(4) and 0.21(3) mm/s and quadrupole splittings of 0.89(6) and
0.53(7) mm/s, respectively, were observed.
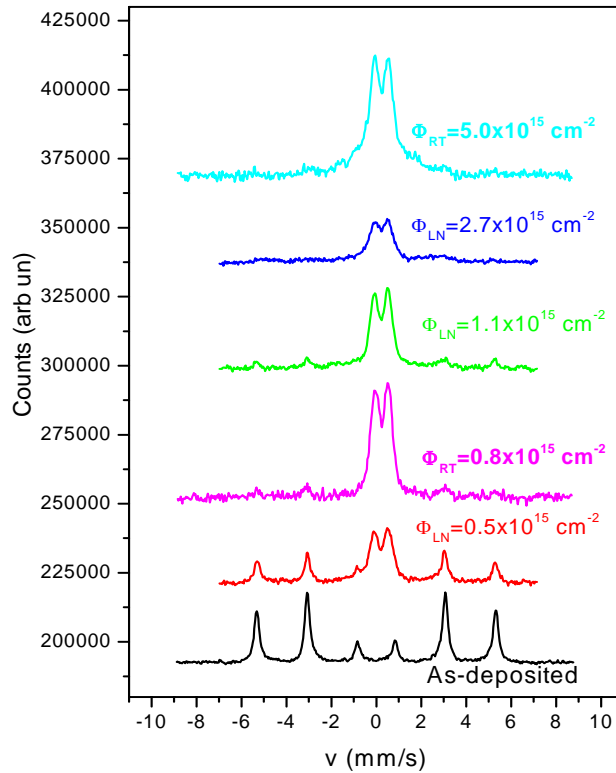
Figure 6.2.6 CEM spectra of the as-deposited and irradiated
samples.
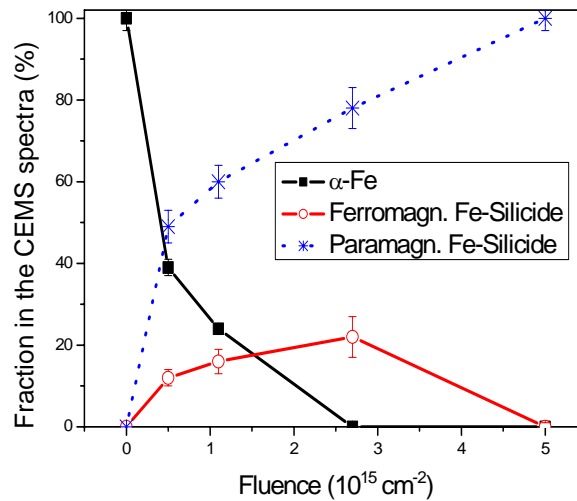
Figure 6.2.7 Evolution of the relative fraction of the amorphous
ferromagnetic and paramagnetic phase and the crystalline α-Fe phase for
different irradiation fluences.

Figure 6.2.7 presents the evaluation of the ferromagnetic and paramagnetic contributions to the spectra.

The transformation from the ferromagnetic crystalline α-Fe and amorphous Fe-silicide phase to the paramagnetic Fe-silicide phases indicates an increasing presence of silicon atoms in the vicinity of ^{57}Fe. The counting statistics was not sufficient to dissolve particular paramagnetic phases.

Comparing the CEMS results with those obtained by XRD measurements it can be concluded that crystalline iron remains on the surface (i.e. on the layer of natural iron), while the region close to the iron/silicon interface is completely mixed and amorphous, in the interface region there is ^{57}Fe, and the CEMS results come from this region, while the XRD experiments provide data of the whole sample.

Assmann et al. performed a similar CEMS experiment, in which ^{nat}Fe(30 nm)/^{57}Fe (10 nm)/Si trilayers were irradiated with 243 MeV Au, 210 MeV I and 160 MeV Ag ions [6-10]. Two paramagnetic doublets with hyperfine parameters similar to ours were identified and associated with the metastable, high-temperature crystalline α-FeSi$_2$ phase. Also, this group ruled out any solute iron atoms in Si. As can be seen from our RBS results, significant mixing occurs during irradiation with 350 MeV Au ions. The XRD measurements gave no indication of any crystalline phase, and finally CEMS showed the presence of two paramagnetic doublets with a large broadening, indicating the amorphous nature of those iron-silicide(s). The above discrepancy may possibly be attributed to the lower ion energies and fluences ($\leq 5.4 \times 10^{14}$ cm^{-2}) used by Assmann et al.

Similar results were achieved by Bauer, Dufour et al. [6-11], using ^{57}Fe (4.5 nm)/Si (3.5 nm) multilayers, which were irradiated with U (650 MeV), Xe (858 MeV) or Kr (736 MeV) ions up to a fluence of 10^{14} cm^{-2}. An important difference between their and our CEMS results is the relative contribution of the amorphous ferromagnetic phase. At the highest fluence we used (5×10^{15} 1/cm^2) this phase had vanished, while Bauer, Dufour et al. recorded a constant increase in the fraction of this phase with increasing fluence (up to 1×10^{14} cm^{-2}).

For those samples irradiated at a fluence of 0.5×10^{15} cm^{-2} a relative contribution to the CEM spectra was sufficient to record MOMS spectra (see Fig 6.2.8).

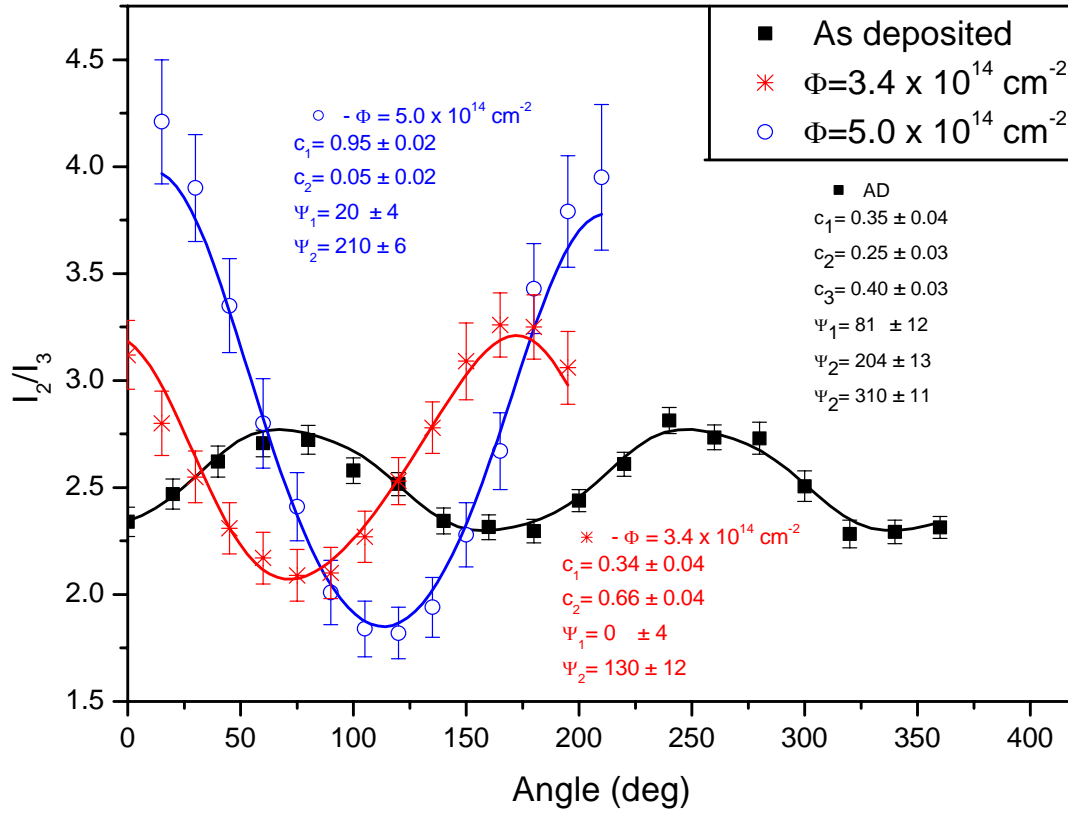Figure 6.2.8 MOMS spectra, and corresponding fits, of the as-deposited sample and of the sample irradiated with 3.4 and 0.5×10^{15} Au-ions/cm^2.

The relative ratio of the intensities of the second and third peak was fitted with the following function [6-13]:

$$\frac{I_2}{I_3} = 4 \sum_{i=1}^{n} c_i \frac{1 - \sin^2 \alpha \sin^2 (\varphi - \Psi_i)}{1 + \sin^2 \alpha \sin^2 (\varphi - \Psi_i)}; \quad \sum_{i=1}^{n} c_i = 1, \quad (6.2.1).$$

Small variations of the I_2/I_3 values in the as-deposited sample indicate the isotropic in-plane spin distribution. In order to fit this spectrum, three terms from Eq. 6.2.1 were used. Almost the same contributions c_i were found and the orientations were separated by approximately 120°. This is a clear sign of near-isotropic distributions of the in-plane spins. With the irradiated sample, the differences in the I_2/I_3 ratios are much more pronounced, and a clear preferential orientation of the spin is present.

The biggest contribution to the CEMS/MOMS spectra comes from the conversion electrons originating from the ^{57}Fe/Si interface region. In order to check the magnetic properties of the near-surface region, MOKE measurements were performed. Figure

6.2.8 shows the results of the MOKE measurements of the samples irradiated up to 1.1×10^{15} cm^{-2}.
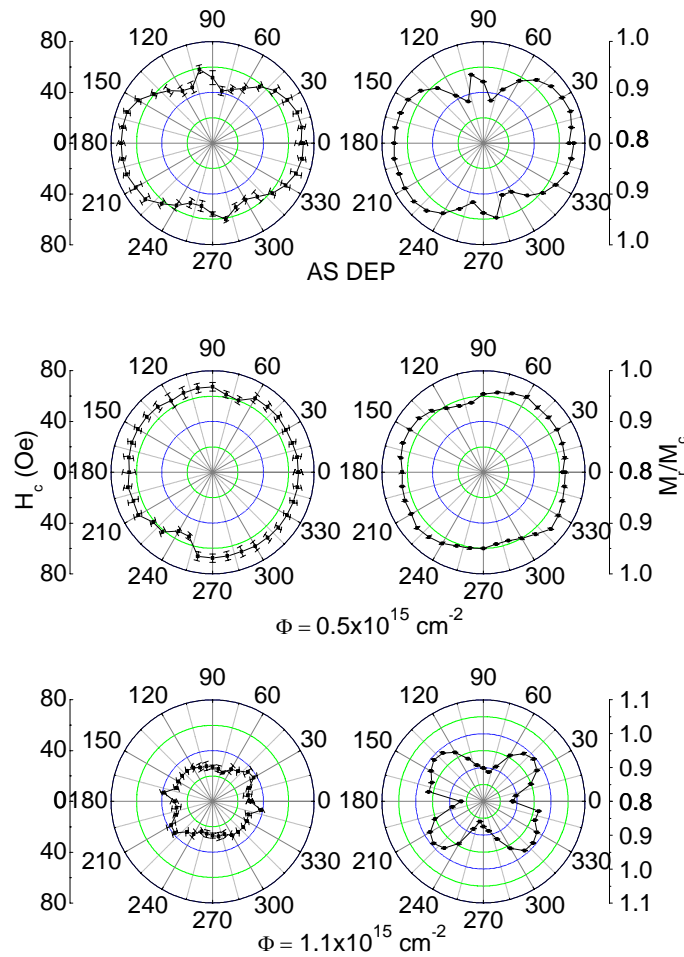
Figure 6.2.8 Fluence dependence of the coercivity field H_c and relative magnetic remanence M_r/M_s obtained by MOKE measurements.

The as-deposited Fe layer shows uniaxial magnetic anisotropy, coupled with a slight fourfold anisotropy. The component with four-fold symmetry grew to 5×10^{14} and 1.1×10^{15} cm^{-2}, but finally isotropic magnetization was found for the highest Au-ion fluences of 2.7 and 5×10^{15} cm^{-2}. These findings differ from the ones achieved by the MOMS technique, which indicates the difference in the structural changes in the surface and the interface region of the samples, which is due to the irradiation with swift heavy ions.

7. References

Chapter 1: Summary

[1-1] V. Milinovic, N. Bibibc, S. Dhar, M. Siljegovic, P. Schaaf, K. P. Lieb, *Appl. Phys. A,* **79** 2093-2097 (2004).

[1-2] N. Bibic, V. Milinovic, S. Dhar, K. P. Lieb, M. Milosavljevic, M. Siljegovic, D. Perusko, P. Schaaf, *Thin Solid Films,* **459** (2004) 23-27.

[1-3] K. P. Lieb, K. Zhang, V. Milinovic, P. K. Sahoo and S. Klaumünzer, *Nucl. Instr. Meth. B* - **in press**

[1-4] V. Milinovic, K. P. Lieb, P. K. Sahoo, P. Schaaf, K. Zhang, S. Klaumünzer and M. Weisheit, *Appl. Surf. Sci.* - **in press**

Chapter 2: Introduction

[2-1] W. D. Cussins, *Proc. Phys. Soc.*, **368** (1955) 213.

[2-2] G. Dearneley, *Nucl. Instr. Meth. B***, 50** (1990) 358.

[2-3] J. Lindhard, M. Scharff, *Mat. Fis. Medd. Dan. Vid. Selsk.,* **33 No. 14**(1963).

[2-4] P. D. Townsend, J. C. Kelly and N. E. W. Hartley, *Ion Implantation, Sputtering and Their Applications,* Academic Press Inc., London (1976).

[2-5] J. F. Ziegler, J. P. Biersack, U. Littmark, *The Stopping and Range of Ions in Solids*, Pergamon Press, New York, 1985.
http://www.srim.org

[2-6] Y. T. Cheng, *Mat. Sci. Rep.,* **5** (1990) 45.

[2-7] P. Sigmund, *Phys. Rev.,* **184** (1969) 383.

[2-8] P. Sigmund and A. Gras-Marti, *Nucl. Instr. Meth.***, 182/183** (1981) 25.

[2-9] W. L. Johnson, Y. T. Cheng, M. van Rossum and M. A. Nicolet, *Nucl. Instr. Meth.***, B 7/8** (1985) 657.

[2-10] P. Borgersen, D. A. Lilenfeld and H. H. Johnson, *Appl. Phys. Lett.,* **57** (1990) 1407

[2-11] G. Rixecker, P. Schaaf, and U. Gonser, *Phys. Stat. Sol. (a)* **139** (1993) 309, and references there-in.

[2-12] P. Mangin and G. Marchal, *J. Appl. Phys.,* **49** (1978) 1709.

[2-13] J. Desimoni and F. H. Sanchez, *Hyp. Int.,* **122** (1999) 277; **113** (1998) 403.

[2-14] M. Milosavljevic, S. Dhar, P. Schaaf, N. Bibic, M. Han, K. P. Lieb, *Appl. Phys. A* **71** (2000) 43.

[2-15] M. Milosavljevic, S. Dhar, P. Schaaf, N. Bibic, M. Han, K. P. Lieb, *Nucl. Instr. Meth.***, B 178** (2001) 4474.

[2-16] P. Schaaf, M. Milosavljevic, S. Dhar, N. Bibic, K. P. Lieb, M. Wölz and G. Principi, *Hyp. Int.,* **139/140** (2002) 615.

[2-17] S. Dhar, P. Schaaf, N. Bibic, E. Hooker, M. Milosavljevic, K. P. Lieb, *Appl. Phys. A* **76** (2003) 773.

[2-18] S. Dhar, P. Schaaf, K. P. Lieb, N. Bibic, M. Milosavljevic, T. Sajavaara, J. Keinonen, A. Traverse, *Nucl. Instr. Meth.***, B 205** (2003) 741.

[2-19] S. Dhar, M. Milosavljevic, P. Schaaf, N. Bibic, K. P. Lieb, "Ion Beam Mixing and silicide formation in Fe/Si and Ta/Si bilayers", Proceedings 21st International Conference and Summer School on the Physics of Ionized Gases

(SPIG2002), August 25-30, 2002, Sokobanja, Belgrade, Yugoslavia, "The Physics of Ionized Gases",
Eds.: N. Bibic, T. Grozdanov, and M. Radovic (Vinca Institute of Nuclear Science, Belgrade, 2003) 189-206.

[2-20] M. Milosavljevic, S. Dhar, P. Schaaf, N. Bibic, Y. L. Huang, M. Seibt, and K. P. Lieb, *J. Appl. Phys.,* **90** (2001) 4474.

Chapter 3: Experimental techniques

[3-1] J. F. Harbsmeier, Dissertation, Göttingen 2000.
[3-2] A. Dobrosavljevic, M. Milosavljevic, N. Bibic, A. Efremov, *Rev. Sci. Instrum.* **71** (2000) 786.
[3-3] H. U. Krebs, *Int. J. Non-Equil. Proc.,* **10** (1997) 3.
[3-4] J. F. Ziegler and W. K. Chu, *Atomic Data and Nuclear Data Tables,* **13** (1974) 463.
[3-5] F. Hubert, A. Fluery, R. Bimbot and H. Gauvin, *Atomic Data and Nuclear Data Tables,* **46** (1990) 1.
[3-6] W. K. Chu, J. W. Mayer, M. A. Nicolet, *Backscattering Spectrometry,* Academic Press, New York, 1978.
[3-7] J. R. Tesmer, M. Nastasi, *Handbook of Modern Ion Beam Materials Analysis,* Material Science Society, Pittsburgh, 1995.
[3-8] K. P. Lieb, *Contemp. Phys.*, **40** (1999) 385.
[3-9] R. L. Doolittle, *Nucl. Instr. Meth. B,* **15** (1986) 227.
      http://www.genplot.com/
[3-10] N. P. Barradas, C. Jeynes, R. P. Webb, *Appl. Phys. Lett.* **71** (1997) 291.
      http://www.ee.surrey.ac.uk/SCRIBA/ibc/ndf/
[3-11] http://www.srim.org/#IBA
[3-12] M. Uhrmacher, K. Pampus, F. J. Bergmeister, D. Purschke, K. P. Lieb, *Nucl. Instr. Meth. B,* **9** (1985) 234.
[3-13] P. Schaaf, A. Krämer, L. Blaes, G. Wagner, F. Aubertin, and U. Gonser, *Nucl. Instr. and Meth.* **B 53** (1991) 184.
[3-14] R. L. Mössbauer, *Z. Physik,* **151** (1958) 124.
[3-15] J. J. Spijkermann, *Conversion Electron Mössbauer Spectroscopy in Mössbauer Effect Methodology,* Vol. 7, I. J. Gruvermann ed., Plenum Press, New York - London, (1981).
[3-16] U. Gonser, *Mössbauer Spectroscopy in Microscopic Methods in Metals*, Springer Verlag (1986).
[3-17] http://www.isapps.ca/recoil/
[3-18] P. Schaaf, C. Illgner, M. Niederdrenk and K. P. Lieb, *Hyp. Int.* **95** (1995) 199-225.
[3-19] P. Schaaf, *Prog. in Mat. Sc.,* **47** (2002) 1.
[3-20] M. Kopcewicz, J. Jagilski, A. Turos, D. L. Williamson, *J. Appl. Phys.,* **71** (1992) 4217.
[3-21] E. U. Concon and G. H. Shortley, *The Theory of Atomic Spectra,* Cambridge Univ. Press, 1935.
[3-22] P. Schaaf, G. A. Müller, E. Carpene and M. Kahle, *Hyp. Int.,* **144/145** (2002) 129.
[3-23] G. A. Müller, R. Gupta, K. P. Lieb and P. Schaaf, *Appl. Phys. Lett.,* **82** (2003) 73.
[3-24] G. A. Müller, doctoral thesis, Göttingen 2004.

http://webdoc.sub.gwdg.de/diss/2004/mueller_georg/

[3-25] M. Faraday, *On the magnetization of light and illumination of magneticlines of force,* Phil. Trans. Royal. Soc. (london) **136** (1846) 1.

[3-26] J. Kerr: *On rotation of the plane of polarization by reflection from the polar of a magnet,* Phil. Mag. **(5) 3** (1877) 321.

[3-27] P. N. Argyres, *Phys. Rev.,* **97** (1955) 334.

[3-28] B. R. Cooper, *Phys. Rev.,* **139** (1965) A1504.

[3-29] A. Hubert and R. Schäfer, *Magnetic domains - the analysis of magnetic microstructures,* Springer - Verlag Berlin Heidelberg, 1998.

[3-30] R. Jenkins and R. L. Snyder, *Introduction to X-ray powder diffractometry*, John Wiley & Sons, Inc., 1996.

[3-31] CD-ROM: PDF-2 Data Base (Sets 1-47), PDF-2 47 6A JUN97; JCPDS - International Center for Diffraction Data.

Chapter 4: Nitrogen irradiation and thermal annealing

[4-1] L. Rissanen, S. Dhar and K. P. Lieb, *Phys. Rev. B* **63** (2001) 155411.

[4-2] R. W. Cahn, P. Haasen, *Physical metallurgy*, Amsterdam/Oxford/New York/Tokio: North-Holland Physics Publishing, 1983.

[4-3] C. R. Brooks, *Principles of the surface treatment of steels*, Lancaster, Basel; Technomic Publishing Company, 1992.

[4-4] J. Kunze, *Nitrogen and carbon in iron and steel*, Berlin; Akademie Verlag, 1990.

[4-5] H. A. Wriedt, N. A. Gokcen, R. H. Nafziger, T. B. Massalski, *Binary alloy phase diagrams*; American Society for Metals (ASM), Metals Park, OH.

[4-6] P. Schaaf, C. Illgner, M. Niederdrenk and K. P. Lieb, *Hyp. Int.* **95** (1995) 199-225; and references there in.

[4-7] H. U. Krebs, *Int. J. Non-Equil. Proc.,* **10** (1997) 3.

[4-8] A. Dobrosavljevic, M. Milosavljevic, N. Bibic, A. Efremov, *Rev. Sci. Instrum.* **71** (2000) 786.

[4-9] M. Kopcewicz, J. Jagielski, A. Turos, D. L. Williamson, *J. Appl. Phys.* **91** (2002) 6465.

[4-10] N. Bibic, V. Milinovic, S. Dhar, K. P. Lieb, M. Milosavljevic, M. Siljegovic, D. Perusko, P. Schaaf, *Thin Solid Films,* **459** (2004) 23-27.

[4-11] Y. T. Cheng, *Mat. Sci. Rep.* **5** (1990) 45.

[4-12] W. Bolse, *Mat. Sci. Eng. R* **12**, 40 (1994); *Nucl. Instr. Meth. B,* **148** (1999) 83.

[4-13] T. Corts, W. Bolse, A. Traverse, *Nucl. Instr. Meth. B,* **80** (1993) 167.

[4-14] S. Dhar, L. Rissanen, K. Engel, M. Wenderoth, K. P. Lieb, *Nucl. Instr. Meth. B,* **178** (2001) 297.

[4-15] V. Milinovic, N. Bibic, S. Dhar, M. Siljegovic, P. Schaaf, K. P. Lieb, *Appl. Phys. A,* **79** (2004) 2093-2097.

[4-16] M. Niederdrenk, P. Schaaf, K. P. Lieb, O. Schulte, *J. Alloys Compd.* **237** (1996) 81.

[4-17] M. J. Clauser, *Solid State Commun.* **8** (1970) 751.

[4-18] J. Desimoni, F. H. Sanchez, *Hyp. Int.* **122** (1999) 277.

Chapter 5: Effects of substrate amorphization and ion charge

[5-1] J. F. Ziegler, J. P. Biersack, U. Littmark, *The Stopping and Range of Ions in Solids*, Pergamon Press, New York, 1985.
http://www.srim.org

[5-2] A. Dobrosavljevic, M. Milosavljevic, N. Bibic, A. Efremov, *Rev. Sci. Instrum.* **71** (2000) 786.

[5-3] K. P. Lieb, *Contemp. Phys.*, **40** (1999) 385.

[5-4] N. P. Barradas, C. Jeynes, R. P. Webb, *Appl. Phys. Lett.* **71** (1997) 291.
http://www.ee.surrey.ac.uk/SCRIBA/ibc/ndf/

[5-5] S. Dhar, P. Schaaf, K. P. Lieb, N. Bibic, M. Milosavljevic, T. Sajavaara, J. Keinonen, A. Traverse, *Nucl. Instr. Meth.***, B 205** (2003) 741.

[5-6] N. Stolterfoht, J. H. Bremer, R. D. Muino, *Int. J. Mass. Spectrom.,* **192** (1999) 425.

Chapter 6: Swift ion irradiation with 350 MeV Au ions

[6-1] J. F. Harbsmeier, Dissertation, Göttingen 2000.

[6-2] http://www.hmi.de

[6-3] J. F. Ziegler, J. P. Biersack, U. Littmark, *The Stopping and Range of Ions in Solids*, Pergamon Press, New York, 1985.
http://www.srim.org

[6-4] D. K. Avasthi, W. Assmann, A. Tripathi, S. K. Srivastava, S. Ghosh, F. Grüner and M. Toulemonde, *Phys. Rev. B* **68** (2003) 153106.

[6-5] S. Dhar, P. Schaaf, N. Bibic, E. Hooker, M. Milosavljevic, K. P. Lieb, *Appl. Phys. A,* **76** 773-780 (2003).

[6-6] K. Izui, *J. Phys. Soc. Jpn.* **20** 945 (1965).

[6-7] K. Markele, *Phys. Rev. Lett.* **9** 150 (1962).

[6-8] Z. G. Wang, C. Dufour, E. Paumier, M. Toulemonde, *J. Phys.: Condens Matt.* **6** (1994) 6773.

[6-9] S. Kraft, B. Schattat, W. Bolse, S. Klaumünzer, F. Harbsmeier, A. Kulinska, A. Löffl, *J. Appl. Phys.* **91** (2002) 1129.

[6-10] M. Toulemonde, C. Dufour, E. Paumier, *Phys Rev B* **46** (1992) 14362.

[6-11] W. Assmann, M. Dobler, D. K. Avasthi, S. Kruijer, H. D. Mieskes, H. Nolte, *Nucl. Instr. Meth. B***, 146** (1998) 271.

[6-12] P. Bauer, C. Dufour, C. Jaouen, G. Marchal, J. Pacaud, J. Grilhe, J. C. Jousset, *J. Appl. Phys.* **81** (1997) 116.

[6-13] G. A. Müller, R. Gupta, K. P. Lieb and P. Schaaf, *Appl. Phys. Lett.,* **82** (2003) 73.

Acknowledgements

Of course that I did not forget Dr. Michael Uhrmaher. The list that I am greatfull to him will be long, so I will reduce it to: support, advices, small talks (physic/non physic topics), constant good mood…..

Last but not least, I would like to express the gratitude towards my parents Radosav and Slobodanka Milinović for their encouragement and understanding.

Curriculum Studiorum

Personal Data:
- *name*: Velimir Milinović
- *birthplace*: Belgrade - Serbia and Montenegro
- *birthdate*: 15. 04. 1970
- *citizenship*: Serbian

Education:
- *1977-1985*: Elementary School (Serbia and Montenegro)
- *1985-1989*: High School (Serbia and Montenegro)
- *1989-1990*: Military Service
- *1990-1999*: Physics studies at the University of Belgrade (Serbia and Montenegro)
- *1999-2002*: Master's studies at the University of Belgrade (Serbia and Montenegro)
- *2002-2005*: Physics PhD student at the II. Physikalisches Institut, University of Göttingen (Germany)

Teaching activities
- *2005*: Fortgeschrittenenpraktikum at the II. Physikalisches Institut, University of Göttingen (Germany)